

Stagnation of atmospheric circulation leads to historically prolonged extreme rainfall event over northwestern India in August 2024

Article

Published Version

Creative Commons: Attribution 4.0 (CC-BY)

Open Access

Mahendra, N., Huber, M., Wang, L., Hunt, K. M. R. ORCID: https://orcid.org/0000-0003-1480-3755, Chilukoti, N. and Chowdary, J. S. (2025) Stagnation of atmospheric circulation leads to historically prolonged extreme rainfall event over northwestern India in August 2024. Journal of Geophysical Research: Atmospheres, 130 (21). e2025JD044227. ISSN 2169-8996 doi: 10.1029/2025JD044227 Available at https://centaur.reading.ac.uk/127003/

It is advisable to refer to the publisher's version if you intend to cite from the work. See Guidance on citing.

Published version at: https://agupubs.onlinelibrary.wiley.com/doi/10.1029/2025JD044227
To link to this article DOI: http://dx.doi.org/10.1029/2025JD044227

Publisher: American Geophysical Union

All outputs in CentAUR are protected by Intellectual Property Rights law, including copyright law. Copyright and IPR is retained by the creators or other copyright holders. Terms and conditions for use of this material are defined in



the End User Agreement.

www.reading.ac.uk/centaur

CentAUR

Central Archive at the University of Reading Reading's research outputs online



JGR Atmospheres



RESEARCH ARTICLE

10.1029/2025JD044227

Special Collection:

Extratropical Large-scale Atmospheric Circulation Variability and Extreme Events Across Scales: Understanding, Modeling, and Prediction

Key Points:

- A historical 10-day extreme precipitation event in northwestern India contributed >60% of all-India rainfall in August 2024
- Stagnation of the subtropical circulation, marked by an upstream Atlantic block over Ural Mountains, led to the formation of a jet streak
- Jet streak's ageostrophic circulation steered a low-pressure system into NWI, elevated 500 hPa humidity enabled sustained deep convection

Supporting Information:

Supporting Information may be found in the online version of this article.

Correspondence to:

M. Huber, huberm@purdue.edu

Citation:

Mahendra, N., Huber, M., Wang, L., Hunt, K. M. R., Chilukoti, N., & Chowdary, J. S. (2025). Stagnation of atmospheric circulation leads to historically prolonged extreme rainfall event over northwestern India in August 2024. *Journal of Geophysical Research: Atmospheres, 130*, e2025JD044227. https://doi.org/10.1029/2025JD044227

Received 29 APR 2025 Accepted 15 OCT 2025

Author Contributions:

Conceptualization:

Nimmakanti Mahendra, Matthew Huber Data curation: Nimmakanti Mahendra Formal analysis: Nimmakanti Mahendra Funding acquisition:

Nimmakanti Mahendra, Matthew Huber, Nagaraju Chilukoti

© 2025. The Author(s). This is an open access article under the terms of the Creative Commons Attribution License, which permits use, distribution and reproduction in any medium, provided the original work is properly cited.

Stagnation of Atmospheric Circulation Leads to Historically Prolonged Extreme Rainfall Event Over Northwestern India in August 2024

Nimmakanti Mahendra^{1,2}, Matthew Huber¹, Lei Wang¹, Kieran M. R. Hunt^{3,4}, Nagaraju Chilukoti², and Jasti S. Chowdary⁵

¹Department of Earth, Atmospheric, and Planetary Sciences, Purdue University, West Lafayette, IN, USA, ²Department of Earth and Atmospheric Sciences, National Institute of Technology, Rourkela, India, ³Department of Meteorology, University of Reading, Reading, UK, ⁴National Centre for Atmospheric Science, University of Reading, Reading, UK, ⁵Indian Institute of Tropical Meteorology, Ministry of Earth Sciences, Pune, India

Abstract Northwestern India (NWI) received anomalously heavy rainfall from 21 to 30 August, 2024, despite the monsoon being in a break phase. This study reveals how midlatitude dynamics triggered this unusual event. Using reanalysis, we perform a moisture budget analysis and local wave activity (LWA) diagnostics and find that the enhanced mid-tropospheric baroclinic instability >1.1 day⁻¹ (1.34σ) peaked during 13–17 August in the North Atlantic, 7-10 days before the NWI rainfall event. This instability fueled the North Atlantic westerly jet and reinforced a "Ω" shaped blocking high over the Ural Mountains ("Ural block") that developed over 21-22 August. This block initiated a wave train that propagated eastward with increasing amplitude over subsequent days. The downstream distorted Rossby waves broke, triggering a pronounced Caspian Sea trough that deepened by 25-26 August, strengthening a subtropical jet streak north of the Tibetan Plateau, with maximum geostrophic wind speeds exceeding 120 m s⁻¹. The NWI was in the jet streak's right entrance region, where the upper-level divergence and compensatory upward motion intensified a low-pressure system that had been steered northwestward into the region. Despite monsoon break conditions, the elevated mid-tropospheric humidity allowed sustained deep convection, which combined with the quasigeostrophic ascent arising from the jet streak entrance region and led to extreme rainfall over NWI. Our analysis provides a case study showing the importance of the growing influence of mid-latitude circulation changes traceable to alterations in the North Atlantic for Indian monsoon variability. The physical linkages demonstrated here may be crucial for improving monsoon behavior in changing climate.

Plain Language Summary This study investigates the anomalous rainfall over northwestern India from 21 to 30 August, 2024, which accounted for over 60% of that month's rainfall total over all India. Despite an early August break phase, above-normal monthly rainfall occurred due to the interplay of synoptic-scale tropical and midlatitude dynamics. Our research explains that this event traced its origins to weather patterns beginning in the North Atlantic Ocean. These distant weather disturbances intensified upper-level (200 hPa) winds (jet streams) and created a chain reaction across Eurasia: they strengthened a blocking weather system over the Ural Mountains, triggering the formation of cyclonic circulation to the east of the Caspian Sea. As a result, enhanced subtropical jet streams flowed north of the Tibetan Plateau. These intensified winds caused upper-level divergence with lower-level low pressure beneath over northwestern India, drawing in moisture and resulting in heavy rainfall despite the presence of weak monsoon conditions. This research highlights how stagnation of atmospheric circulation and distant weather systems can significantly influence local rainfall in India, which is crucial for enhancing monsoon predictions on a range of time scales.

1. Introduction

Intraseasonal rainfall variability in the Indian Summer Monsoon (ISM) has been growing increasingly complex in recent decades due to the overarching impacts of climate change, for example, (Bollasina et al., 2011; Rajeevan et al., 2012; Turner & Annamalai, 2012). The ISM plays a critical role in water security, agriculture, and economic stability in India (Gadgil & Gadgil, 2006). Therefore, ISM variability has been the focus of extensive research for over a century. Despite significant improvement, the seasonal forecasting of the ISM is still fraught with uncertainty, primarily due to its variability being sensitive to many modes of large-scale variability across the globe (Bach et al., 2024; Pradhan et al., 2017).

MAHENDRA ET AL. 1 of 29

Investigation: Nimmakanti Mahendra, Matthew Huber

Methodology: Nimmakanti Mahendra, Matthew Huber, Lei Wang, Kieran M. R. Hunt, Nagaraju Chilukoti, Jasti S. Chowdary

Project administration:

Nagaraju Chilukoti

Resources: Matthew Huber Software: Nimmakanti Mahendra Supervision: Matthew Huber Validation: Matthew Huber, Lei Wang, Kieran M. R. Hunt, Nagaraju Chilukoti, Jasti S. Chowdary

Visualization: Nimmakanti Mahendra,

Nagaraju Chilukoti Writing – original draft: Nimmakanti Mahendra

Writing – review & editing:

Nimmakanti Mahendra, Matthew Huber, Lei Wang, Kieran M. R. Hunt, Nagaraju Chilukoti, Jasti S. Chowdary Recent years have witnessed contrasting rainfall trends across India: increased rainfall over Northwest India (NWI) versus decreasing rainfall over the Indo-Gangetic plains/Central Indian region (CI), leading to flash floods and droughts, respectively (Goswami et al., 2006; Kulkarni et al., 2020; Mahendra et al., 2023; Singh et al., 2022; Yadav, 2024). These changing patterns have been attributed to decreasing monsoon depressions over the Bay of Bengal (Mahendra et al., 2023; Vishnu et al., 2016), particularly an uptick in northern Arabian Sea depressions (Chilukoti et al., 2024); changing atmospheric circulation patterns such as the easterly low-level jet across the Indo-Gangetic Plains during peak monsoon season (Acosta & Huber, 2017) with emphasis on upper-level vorticity anomalies and mid-tropospheric instability (Mishra et al., 2024); and potential teleconnections with Indian Ocean warming and shifting jet stream patterns (Mahendra et al., 2024; Vibhute et al., 2023; L. Wang et al., 2017).

Historically, around 50% of the predictive power for ISM rainfall has been attributed to large-scale climate drivers, with the El Niño-Southern Oscillation (ENSO) being the most prominent; its influence on the monsoon is extensively studied and well documented across various time scales, for example, (Chowdary et al., 2021; Goswami & Xavier, 2005; Kripalani & Kulkarni, 1997; Webster & Yang, 1992). However, some studies have shown that the relationship between ENSO and the ISM has become increasingly nonlinear (Krishnamurthy & Goswami, 2000; Kumar et al., 1999) and region-specific in recent decades (Athira et al., 2023; Mahendra et al., 2021). This shift is driven by the growing influence of other climate phenomena, such as the Indian Ocean Dipole (IOD) (Ashok et al., 2001; Feba et al., 2019), Atlantic Niño (Pottapinjara et al., 2014; Yadav et al., 2018), and midlatitude interactions, which have introduced additional sources of variability in the monsoon system (Ding & Wang, 2005; Goswami et al., 2022; Mahendra et al., 2024; Kosaka & Nakamura, 2010; Vellore et al., 2016; L. Wang et al., 2017). Particularly, in summer, midlatitude Rossby waveguides embedded within the westerly jet streams across Eurasia, known as the Silk Road pattern, have started to play a more significant role in modulating ISM rainfall (Mahendra et al., 2024; Vibhute et al., 2023; L. Wang et al., 2017; Yadav, 2024), complicating the prediction of seasonal monsoon rainfall in recent decades.

This circulation change is attributed to pronounced warming observed in the Northern Hemisphere, particularly in the Arctic regions, and may significantly affect the upper westerly jet stream through a mechanism known as Arctic amplification (Coumou et al., 2018). As demonstrated by Cohen et al. (2018) and Barnes and Screen (2015), the reduced temperature gradient between midlatitudes and polar regions weakens the thermal wind that drives the jet stream, potentially causing it to meander more and adopt a wavier, less zonal pattern. This increased waviness can lead to persistent weather extremes as atmospheric blocking patterns become more common. The notable sea surface temperature (SST) anomalies in the North Pacific and parts of the Atlantic may further complicate this dynamic by altering storm tracks and creating regions of enhanced baroclinicity that locally strengthen or weaken jet segments.

While these broader teleconnection patterns explain interannual variability and aforementioned studies are limited to interannual time scales, how the extratropics influence low-latitude regions on a subseasonal (synoptic) scale is not well understood. Specifically, how the highly energetic extratropical transients affect tropical systems such as monsoons remains an essential question and motivation for this study. Recent studies have increasingly recognized the significant role of midlatitude circulation patterns in modulating monsoon dynamics, particularly for extreme precipitation events in NWI (Hunt, 2024; Hunt et al., 2018a; Vellore et al., 2014). The subtropical westerly jet stream, positioned to the north of the Tibetan Plateau during summer months, can interact with the tropical easterlies in ways that enhance moisture convergence and vertical motion (Bordoni & Schneider, 2008; Krishnan et al., 2009). These interactions can be particularly pronounced during the early and late monsoon seasons when the subtropical jet is at its closest proximity to the monsoon domain (Ding & Wang, 2007; Krishnamurti et al., 2010).

These midlatitude interactions manifest concretely through specific synoptic systems. Western disturbances (WDs), which are mid-latitude synoptic-scale systems that propagate eastward along the subtropical westerly jet, have been traditionally associated with winter precipitation over NWI (Dimri et al., 2015). Yet, there is growing evidence that summer WDs can significantly impact monsoon rainfall patterns when they interact with tropical disturbances (Madhura et al., 2015). These interactions often involve complex Rossby wave dynamics, including wave-breaking events that can lead to persistent atmospheric blocking patterns and extreme precipitation (Martius et al., 2013; Parker et al., 2016).

MAHENDRA ET AL. 2 of 29

The dynamics underlying these WD interactions are often governed by specific wave processes. The role of Rossby wave breaking (RWB) in extreme weather events has been extensively studied in the context of European and North American climate (H. Nakamura & Wallace, 1993; Woollings et al., 2008), but its influence on the ISM has received comparatively less attention. Recent works by Vellore et al. (2016), Hunt et al. (2021), Mahendra et al. (2023) and Saini and Attada (2024) have pointed at and begun to address this gap, Roxy et al. (2017) suggesting that RWB events, which include WDs, can trigger northward excursions of tropical moisture, creating atmospheric rivers that deliver extreme rainfall to northern India. Furthermore, studies by Priya et al. (2017), Krishnan et al. (2020) and Mahendra et al. (2024) have highlighted how changing patterns of midlatitude circulation may alter the frequency and intensity of such tropical midlatitude interactions in a warming climate.

These emerging insights into RWB mechanisms have contributed to broader scientific debates about extreme rainfall drivers. The scientific debate remains active, with various attributions for recent events. Some emphasize tropical influences in the 2022 Pakistan flooding (Nanditha et al., 2023; Xie et al., 2024), while others highlight large-scale circulation patterns like European and Russian blocking systems (Hunt et al., 2018b; Yuan et al., 2023). When midlatitude waves interact with the monsoon, they can be either reflected or absorbed, significantly modifying the monsoon trough's structure (Hunt et al., 2021) and strengthening monsoon flow along India's western coast.

To develop a better understanding of the relative importance of these many processes, it is useful to focus on an illustrative case study. We chose the recent and highly unusual rainfall event over India in August 2024 because it presents an ideal opportunity to examine these competing hypotheses, as it exemplifies the complex interplay where neither conventional monsoon dynamics nor isolated extratropical influences alone explain the observed patterns.

In August 2024, rainfall over India was above normal, associated with an unusual low-pressure system that made progress toward Gujarat, even though the monsoon appeared to be in a break phase (see Figures S1 and S2 in Supporting Information S1). The break phase is characterized by a northward shift of the monsoon trough and reduced rainfall over CI, while enhanced precipitation occurs over the Himalayan foothills and northeastern regions (Bhatla et al., 2004; Gadgil & Joseph, 2003; Rajeevan et al., 2010). During break periods, weakened low-level circulation leads to suppressed convection over the core monsoon zone. Interestingly, this break phase was reflected in the circulation patterns, with the monsoon trough shifting westward—but not in the thermodynamics—as the mid-troposphere remained relatively humid.

This raises a critical question: what caused this sudden shift in circulation and formation of a low-pressure system, and how did it sustain anomalously high rainfall despite the apparent break phase? The goal of this study is to answer this question.

To answer this question, we conduct a comprehensive analysis of synoptic and dynamic conditions within the context of the various competing explanations described above. We explore key contributing factors, including the monsoon trough's interaction with midlatitude systems, the unusual behavior of westerly troughs, Rossby wave dynamics, persistent atmospheric blocking patterns, and tropical disturbances. The resulting analysis reveals a synergistic interaction between tropical and extratropical systems that amplifies both rainfall intensity and spatial extent, similar to mechanisms observed during the 2010 Pakistan floods (Lau & Kim, 2012) and the 2013 Uttarakhand disaster (Dimri et al., 2015), and we draw upon insights from those studies in our analysis.

The rest of the paper is organized as follows: Section 2 describes the data set and diagnostics methods employed. Section 3 presents the results, discussion, and the implications of our findings for understanding monsoon-midlatitude interactions in a changing climate. Section 4 summarizes the key findings and suggests directions for future research on tropical-extratropical teleconnections affecting ISM.

2. Data and Methodology

2.1. Data

In this study, we use high-resolution gridded rainfall from the India Meteorological Department (IMD) (Pai et al., 2014) and the NOAA Climate Prediction Center (CPC) provided at a daily frequency (M. Chen et al., 2008). To understand the physical mechanisms driving these rainfall patterns, we analyze associated meteorological

MAHENDRA ET AL. 3 of 29

conditions using meteorological variables from ERA5 (European Center for Medium-Range Weather Forecasts) reanalysis data (Hersbach et al., 2023). These include zonal, meridional, and vertical wind components $(u, v, and \omega)$, relative and specific humidity (q), 2-m temperature, and temperature on pressure levels. In addition, vertically integrated variables such as heat transport and kinetic energy are used. These data sets are available at hourly intervals with a 25-km spatial resolution. National Oceanic and Atmospheric Administration (NOAA) Optimum Interpolation (OI) SST Version 2 (V2) 25 km Resolution data were utilized (B. Huang et al., 2021).

2.2. Methodology

Since this work focused on understanding the NWI extreme rainfall event, it is important to understand the recent changes in NWI rainfall through its contribution to the total all-India rainfall. To quantify the contribution of NWI (20°N–30°N, 68°E–78°E), and CI (18°N–28°N, 78°E–88°E) rainfall to the total Indian rainfall in recent decades and specifically for 2024, we used the following approach. Contribution is the ratio between the sum rainfall over all grid points in the chosen region (e.g., NWI or CI) to the sum rainfall over the entire Indian region as a percentage.

Region-Contribution (%) =
$$\left(\frac{\sum_{\lambda,\phi \in \text{Region}} r(\lambda,\phi)}{\sum_{\lambda,\phi \in \text{All India}} r(\lambda,\phi)}\right) \times 100$$
 (1)

Here, r is rainfall at ϕ -latitude, λ -longitude point. To isolate different temporal scales in the data, we apply a Lanczos filter (Duchon, 1979): <10 days (synoptic scale), 10–20 days (quasi-biweekly), 20–90 days (intraseasonal), and >90 days (seasonal to interannual). Application of the Lanczos filter, described in Duchon (1979), is a standard technique in atmospheric sciences, and these bands align with studies on monsoon variability (Krishnamurthy & Goswami, 2000).

We compute moisture budget components based on the methodology of Lubis et al. (2023) using the following equation:

$$\left\langle \frac{\partial q}{\partial t} \right\rangle = -\underbrace{\left\langle \mathbf{V}_H \cdot \nabla q \right\rangle}_{\text{vert.int.horiz.adv.}} - \underbrace{\left\langle q \nabla \cdot \mathbf{V}_H \right\rangle}_{\text{vert.int.horiz.conv.}} - \underbrace{\left\langle \frac{\partial (\omega q)}{\partial p} \right\rangle}_{\text{vert.int.vert.conv.}} - \underbrace{\left\langle \frac{Q_2}{L} \right\rangle}_{\text{source/sink}}$$
(2)

$$Q_2 = -L \left(\frac{\partial q}{\partial t} + \mathbf{V} \cdot \nabla q + \omega \frac{\partial q}{\partial p} \right) \tag{3}$$

The first and second terms are horizontal (H) moisture advection and convergence by zonal (u) and meridional (v) winds. The third and fourth terms explain vertical (w) moisture convergence variations in specific humidity (q), sink (Q_2) , L latent heat of vaporization, and angular brackets represent vertical integration from the surface to 300 hPa.

However, considering that dynamic processes play a major role in vertical motion, it may not be valid to neglect vertical velocity gradients when decomposing $-\frac{\partial (wq)}{\partial p}$. The full decomposition should account for both terms:

$$-\frac{\partial(wq)}{\partial p} = -q\frac{\partial w}{\partial p} - w\frac{\partial q}{\partial p} \tag{4}$$

Moreover, in the lower troposphere, vertical advection dominates due to high moisture content and strong gradients (T. C. Chen et al., 2000; Hagos et al., 2010; Trenberth et al., 2011). Thus, $-\frac{\partial(wq)}{\partial p}$ decomposition should account for both terms:

$$-\left(w\frac{\partial q}{\partial p}\right) = \underbrace{-\Delta\omega\frac{\partial q_0}{\partial p}}_{\text{dynamic}} + \underbrace{-\omega_0\Delta\frac{\partial q}{\partial p}}_{\text{thermodynamic}},\tag{5}$$

MAHENDRA ET AL. 4 of 29

where q_0 and ω_0 are climatologies of specific humidity and vertical velocity, and the first term represents the dynamic component (related to vertical velocity gradients) and the second term represents the thermodynamic component (related to moisture gradients). Given the significant role of dynamic processes in vertical motion, both components should be retained for accurate analysis (Seager et al., 2010; Trenberth et al., 2011). We then estimated the apparent heat source, Q_1 , using the formula given by Yanai et al. (1973), Saini and Attada (2024) as follows.

$$Q_1 = C_p \left(\frac{p}{p_0}\right)^k \left(\frac{\partial \theta}{\partial t} + \mathbf{V} \cdot \nabla \theta + \omega \frac{\partial \theta}{\partial p}\right),\tag{6}$$

where Q_1 represents the apparent heat source in the atmosphere, C_p is the specific heat at constant pressure, $(p/p_0)^{\kappa}$ is the pressure normalization factor with $\kappa = R/C_p$, $\partial\theta/\partial t$ denotes the local rate of change of potential temperature, $\mathbf{V} \cdot \nabla \theta$ represents the horizontal advection of potential temperature, and $\omega \partial\theta/\partial p$ is the vertical advection of potential temperature. We also calculated the moisture backward trajectory using a forward Euler method (Biswas et al., 2013; Stohl, 1998). For backward trajectories, the time step is negative, effectively computing: \vec{x} is the position vector (longitude, latitude, pressure), \vec{v} is the velocity vector (u, v, w), and Δt is the time step along with this 850 to 500 hPa level averaged maximum vorticity paths contracted.

$$\vec{x}_{t-\Delta t} = \vec{x}_t - \vec{v}_t \cdot \Delta t,\tag{7}$$

To measure baroclinic instability, which quantifies the potential for midlatitude waves (eddies) to grow due to vertical wind shear and static stability (Charney, 1947; Eady, 1949; Hoskins & Valdes, 1990; Lindzen & Farrell, 1980), we use the Eady growth rate, σ , defined as follows:

$$\sigma = 0.31 \cdot f \cdot \frac{\partial u}{\partial z} \cdot \frac{1}{N}.$$
 (8)

here, $f = 2\Omega \sin(\phi)$ is the Coriolis parameter, and $\partial u/\partial z$ is the vertical wind shear representing the change in zonal wind speed with height. $N = \sqrt{g/\theta \cdot \partial \theta/\partial z}$ is the Brunt-Väisälä frequency, which represents the static stability of the atmosphere, where g is the gravitational acceleration, θ is the potential temperature, and $\partial \theta/\partial z$ is the vertical gradient of potential temperature.

Following this, C. S. Y. Huang and Nakamura (2016) proposed a Rossby wave dynamics diagnostics method which relies on finite-amplitude local wave activity (LWA).

$$\tilde{A}^*(\lambda, \phi, z, t) = -\frac{a}{\cos \phi} \int_0^{\Delta \phi} q_e(\lambda, \phi, \phi', z, t) \cos(\phi + \phi') d\phi', \tag{9}$$

where \tilde{A}^* is the LWA, a is the Earth's radius, z represents pressure pseudo-height, t is time, and q_e denotes the quasi-geostrophic potential vorticity (QGPV) equivalent latitude. The integration variable ϕ' represents the meridional displacement of QGPV contours from their reference latitude. The $\cos(\phi+\phi')$ factor accounts for the spherical geometry, ensuring proper area weighting. The negative sign establishes the convention where positive LWA corresponds to the poleward displacement of QGPV contours. This formulation preserves wave activity conservation principles while providing spatially resolved information about wave properties, unlike traditional Eliassen-Palm diagnostics, which only provide zonal averages (C. S. Y. Huang & Nakamura, 2016; N. Nakamura & Solomon, 2010; L. Wang & Nakamura, 2015).

The equation below, derived by Mak and Cai (1989), quantifies how eddies extract kinetic energy from (or return energy to) the mean flow through interactions with horizontal wind shear.

$$C(K_Z, K_E) = -\overline{u'u'}\frac{\partial \bar{u}}{\partial x} - \overline{u'v'}\frac{\partial \bar{u}}{\partial y} - \overline{u'v'}\frac{\partial \bar{v}}{\partial x} - \overline{v'v'}\frac{\partial \bar{v}}{\partial y},\tag{10}$$

MAHENDRA ET AL. 5 of 29

where $C(K_Z, K_E)$ represents the barotropic energy conversion between zonal mean kinetic energy (K_Z) and eddy kinetic energy (K_E) , $\overline{u'u'}$, $\overline{u'v'}$, and $\overline{v'v'}$ are the components of the Reynolds stress tensor, and $\frac{\partial \bar{u}}{\partial x}$, $\frac{\partial \bar{v}}{\partial y}$, $\frac{\partial \bar{v}}{\partial x}$, $\frac{\partial \bar{v}}{\partial y}$ are the gradients of the mean flow, where (-) denotes the time mean and (') denotes anomalies. While the barotropic energy conversion quantifies the horizontal exchange between eddy and mean kinetic energy, we also need to understand the meridional mass transport that accompanies these energy exchanges. An element of northward mass flux (in units of kg s⁻¹) across a latitude line is $d\psi = a \cos \phi d\lambda v \frac{dp}{g}$. Zonally and time-averaged mass conservation in pressure coordinates ($[\bar{v}]$) is given by

$$\psi = \frac{2\pi a \cos \phi}{g} \int_0^p \left[\overline{v} \right] dp \tag{11}$$

here, ψ (ϕ ,p) (units of kg s⁻¹) is equal to the rate at which mass is transported meridionally between the surface and 100 hPa.

3. Results and Discussion

3.1. Rainfall Distribution

The changing spatial distribution of Indian monsoon rainfall and the anomalous events of August 2024 are illustrated in Figure 1. The probability density functions in Figures 1a and 1b illustrate the evolving distribution of NWI contribution to overall Indian rainfall across different time periods. The solid red area (1981–2000) shows a distribution centered around 14%, while the orange area (2001–2024) shifts rightward to 16%, indicating a significant increase in NWI's rainfall contribution. The yellow distribution (2019–2024) moves further right to 18%, demonstrating an acceleration in the trend (5.22%/44 years, $R^2 = 0.31$, p < 0.001) during recent years. Most notably, the vertical red dashed line marks the 2024 contribution at 20%, which falls at the extreme right tail of historical distributions. This progressive shift rightward aligns with findings from Pai et al. (2015), who documented changing spatial patterns in the Indian monsoon, with northwestern regions experiencing increasing rainfall intensity relative to historical norms.

Figures 1a and 1b display CI rainfall contribution distribution with higher baseline percentages. The solid blue area represents the 1981–2000 period (35%), the striped blue pattern shows a decline during 2001–2024 (34%), and the light blue indicates further reduction during 2019–2024 (33%). The red vertical line marks the 2024 event at 33%. Unlike NWI, CI shows a slight decreasing trend (-3.07%/44 years, $R^2 = 0.13$, p = 0.015) in the contribution percentage over time, which contextualizes the findings of Roxy et al. (2017) on the spatial redistribution of monsoon rainfall under changing climate conditions in recent years. The contrasting trends between NWI and CI suggest a potential northwestward shift in the focus of monsoon precipitation. CI, traditionally a dominant contributor to monsoon rainfall, shows a declining trend in its contribution, in line with high emission future climate projections (CarbonBrief, 2021). This shift indicates a potential redistribution of monsoon rainfall patterns, raising important questions about regional water security, agricultural planning, and adaptation strategies for water resource management.

Figure 1c shows rainfall charts covering the monsoon 2024 anomaly. When NWI rainfall from 21 to 30 August is removed from calculations, the all-India rainfall for this period shows a prolonged break monsoon condition (bars in Figure 1c). This highlights the localized nature of regional monsoon rainfall disturbances, as proposed by Vellore et al. (2016), where localized circulation features can override the broader monsoon pattern. The spatial map in Figure 1d displays rainfall anomalies across India during the 10-day event period. The deep green shading over NWI (marked by the red box) indicates extreme positive anomalies exceeding 8 mm day⁻¹ above normal. Surrounding regions show near-normal or below-normal rainfall, further emphasizing the localized nature of the event. This spatial pattern resembles the precipitation dipole often associated with tropical-extratropical interactions documented by Priya et al. (2017), Mahendra et al. (2024), where enhanced rainfall in one region occurs simultaneously with suppressed rainfall elsewhere due to compensating atmospheric circulation.

The twin panels (Figures 1e and 1f) present the daily rainfall evolution using two different data sets (IMD and CPC, respectively) to confirm data reliability. The red bars show actual rainfall amounts in 2024, dramatically exceeding the yellow climatological bars during the event period. The lower sections decompose rainfall

MAHENDRA ET AL. 6 of 29

2169896, 2025, 21, Downloaded from https://agupubs.oni.neibbrary.wiley.com/doi/10.1029/2025/ID044277 by Kieran Hunt - NICE, National Institute for Health and Care Excellence, Wiley Online Library on [07/11/2025]. See the Terms and Conditions (thrps://onlinelibrary.wiley.

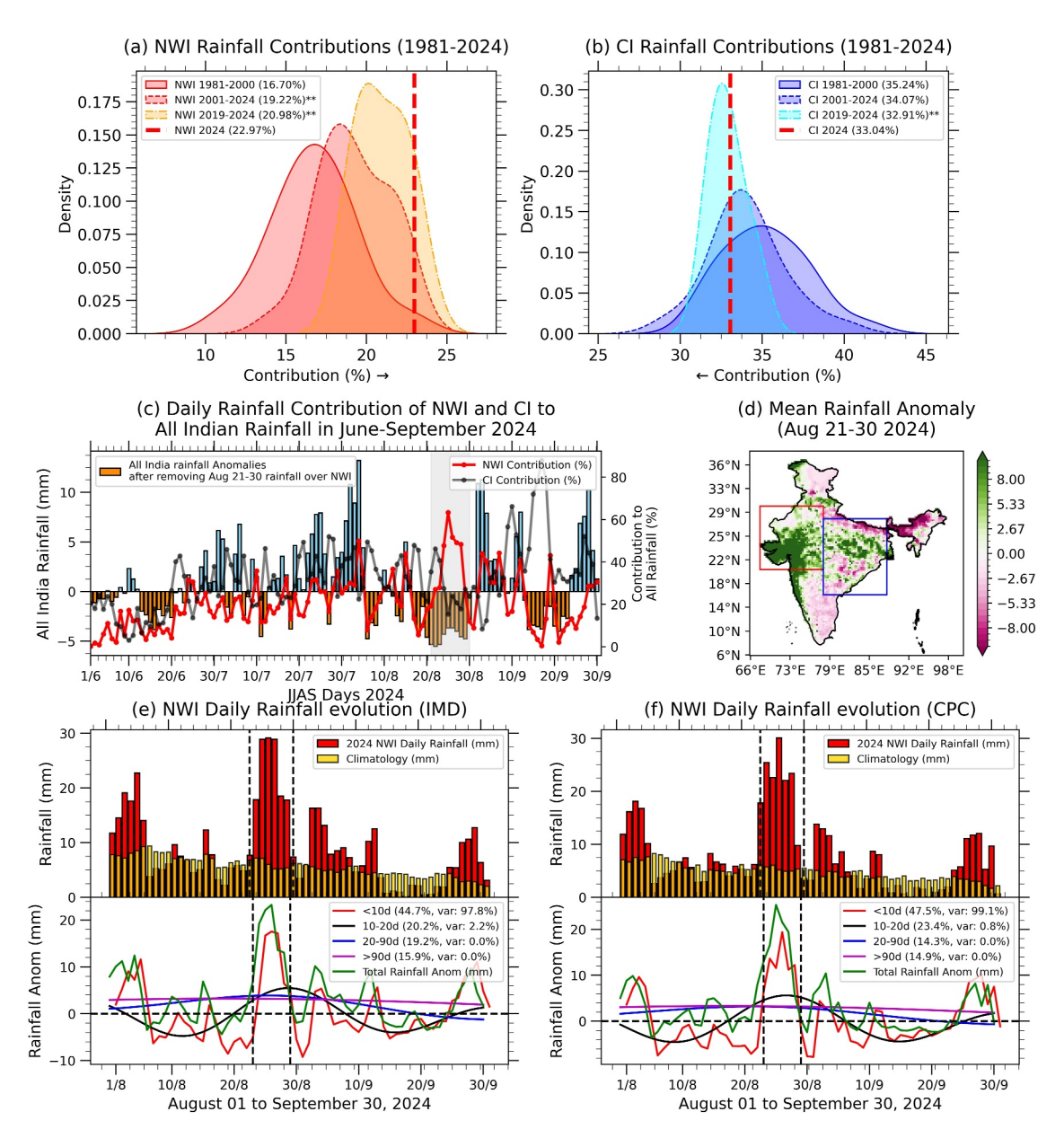


Figure 1. (a, b) Frequency distribution of JJAS mean rainfall contributions (%) from North-West India (NWI:20°N–30°N, 68°E–78°E, red box) and central India (CI:18°N–28°N, 78°E–88°E, blue box) to total all-India rainfall for the periods 1981–2000, 2001–2024, 2019–2024, and 2024 individually marked by double asterisks represents the significance at p < 0.01 using student t-test. (c) All-India JJAS rainfall anomalies (mm day⁻¹) after removing NWI rainfall during 21–30 August. Black and red lines indicate CI, NWI, and their respective contributions to the total all-India rainfall without removing the NWI rainfall from 21 to 30 August. (d) The spatial pattern of rainfall anomalies (mm day⁻¹) for the same period (21–30 August 2024) is highlighted in (c). (e, f) Daily actual rainfall (mm day⁻¹) in August 2024 (red bars) compared with climatology from 1981 to 2010 (orange bars) based on IMD and CPC data. The lower panels show rainfall anomalies ((mm day⁻¹, green) decomposed into different time scales: synoptic (<10 days, red), quasi-biweekly (10–20 days, black), intraseasonal (20–90 days, blue), and seasonal/interannual (>90 days, magenta), labels showing contribution and variance percentages respective bands.

anomalies into different frequency bands: <10 day (synoptic scale, red), 10–20 days (quasi-biweekly, black), 20–90 days (intraseasonal, blue), and >90 day (longer modes of variability, magenta). The green total anomaly line peaks sharply during the event, with the red <10 day band showing the strongest positive contribution. This frequency decomposition supports Hunt et al. (2021)'s conclusion that synoptic-scale processes, particularly those associated with westerly disturbances, are increasingly important for extreme precipitation events in NWI. The strong dominance of synoptic-scale variability during this period, contributing over 60% of the total rainfall, is further supported by the prevalence of <10 day filtered outgoing long wave radiation (OLR), vertical velocity,

MAHENDRA ET AL. 7 of 29

and rainfall anomalies (Figures S3 and S4 in Supporting Information S1). Having established the exceptional nature and synoptic-scale dominance of this rainfall event, we next examine the moisture budget components to understand the advection, convergence, and vertical transport processes that enabled such extreme precipitation.

3.2. Moisture Transport and Budget Analysis

This moisture budget components time series tracks the daily evolution of moisture processes during August–September 2024 (Figure 2a). The yellow bars represent daily rainfall anomalies, with large positive values corresponding to major rainfall events. Individual moisture budget components are represented by colored lines: blue for total moisture budget, pink for horizontal moisture advection, red for horizontal moisture convergence, black for vertical moisture convergence ($-\partial(q\omega)/\partial p$), and green for moisture sink. The maximum values around 25–27 August indicate that vertical moisture convergence (black line) dominated during the event (300 × 10⁵ g kg⁻¹ s⁻¹) and diabatic processes played a major role in enhancing precipitation, as reflected in moisture sink (Q_2). This pattern differs from typical monsoon rainfall events described by Rajeevan et al. (2010), where horizontal moisture convergence often dominates, emphasizing how this atmospheric configuration represents a departure from usual monsoon dynamics. Subsequently, we applied time filtering to the vertical term.

Figure 2b provides a detailed breakdown of the normalized vertical moisture convergence term into its component parts. The dominant contribution comes from the green line, peaking at approximately 3.5 during 25–27 August, which indicates that anomalous vertical motion acting upon the background moisture profile was the primary driver of the heavy rainfall. This finding supports the mechanism proposed by Karmakar et al. (2022); Saini and Attada (2024) and Chilukoti et al. (2024), whereby midlatitude dynamical forcing can generate enhanced vertical velocities that efficiently convert existing atmospheric moisture into precipitation, even during monsoon break phases when the background moisture field remains relatively abundant despite reduced horizontal transport. The domination of synoptic-scale processes (<10 day band) suggests that midlatitude dynamical interaction might have overridden monsoon break conditions to drive the extreme rainfall event. Hereafter, we use raw six-hourly data without any filtering applied.

3.3. Dynamic Vertical Moisture Advection and Diabatic Heating

Figure 3 presents the evolution of dynamic vertical moisture advection and diabatic heating during the event (Equation 6) through latitude-pressure cross-sections spanning 0°-40°N. Building on our earlier analysis of moisture budget, these vertical cross-sections provide crucial insights into the vertical processes that drove this extreme rainfall event. 21-22 August shows a concentrated region of positive forcing between 10°N-20°N extending from 700 to 300 hPa with positive rainfall anomalies reaching approximately 20 mm day⁻¹ around 20°N (Figure 3a). The black contours indicate moderate heating values with respect to a maximum of around 35 K day⁻¹. This early pattern demonstrates what Murthy and Boos (2018) term the "precursor moistening phase", where mid-tropospheric humidity increases before intense convection develops. The modest vertical extent and intensity align with observations in Moron et al. (2009) on the initialization of extreme precipitation events in monsoonal regions. During 23-24 August, the positive forcing strengthens and expands between 15°N-25°N, with maximum values exceeding 9.6 mm day⁻¹ in complement to rainfall shifting further north and intensifying to 40 mm day⁻¹ (Figure 3b). Heating contours become more concentrated, indicating moisture convergence within the column. Concurrently, a region of negative forcing develops north of 25°N, establishing the dipole structure characteristic of enhanced local meridional circulation as described by Vellore et al. (2016). This organizational pattern corresponds to the "coupling phase" in which monsoon LLJ dynamics and moisture transport are conducive to enhanced convective activity and heavy rainfall formation (Xavier et al., 2018).

The 25–26 August period reveals vertical moisture advection maximum forcing intensity centered at $\approx 20^{\circ}$ N with values exceeding 18.2 mm day⁻¹. The vertical column of positive forcing now extends from near-surface (850 hPa) to upper levels (200 hPa), indicating complete tropospheric coupling (Figure 3c) and resulting in widespread rainfall anomalies evident with >50 mm day⁻¹, with the most intense precipitation aligned with the core of dynamic forcing. Heating contours show maximum concentration (32 K day⁻¹), representing strong moisture availability. This structure exemplifies the "vertically coupled deep convection" mechanism identified by Houze et al. (2017) during extreme precipitation events over the Indian subcontinent. By 27–28 August, the system begins transitioning as the core of positive forcing weakens and shifts slightly northward (Figure 3d). The

MAHENDRA ET AL. 8 of 29

for Health and Care Excellence, Wiley Online Library on [07/11/2025]. See the Terms and Conditions (https://

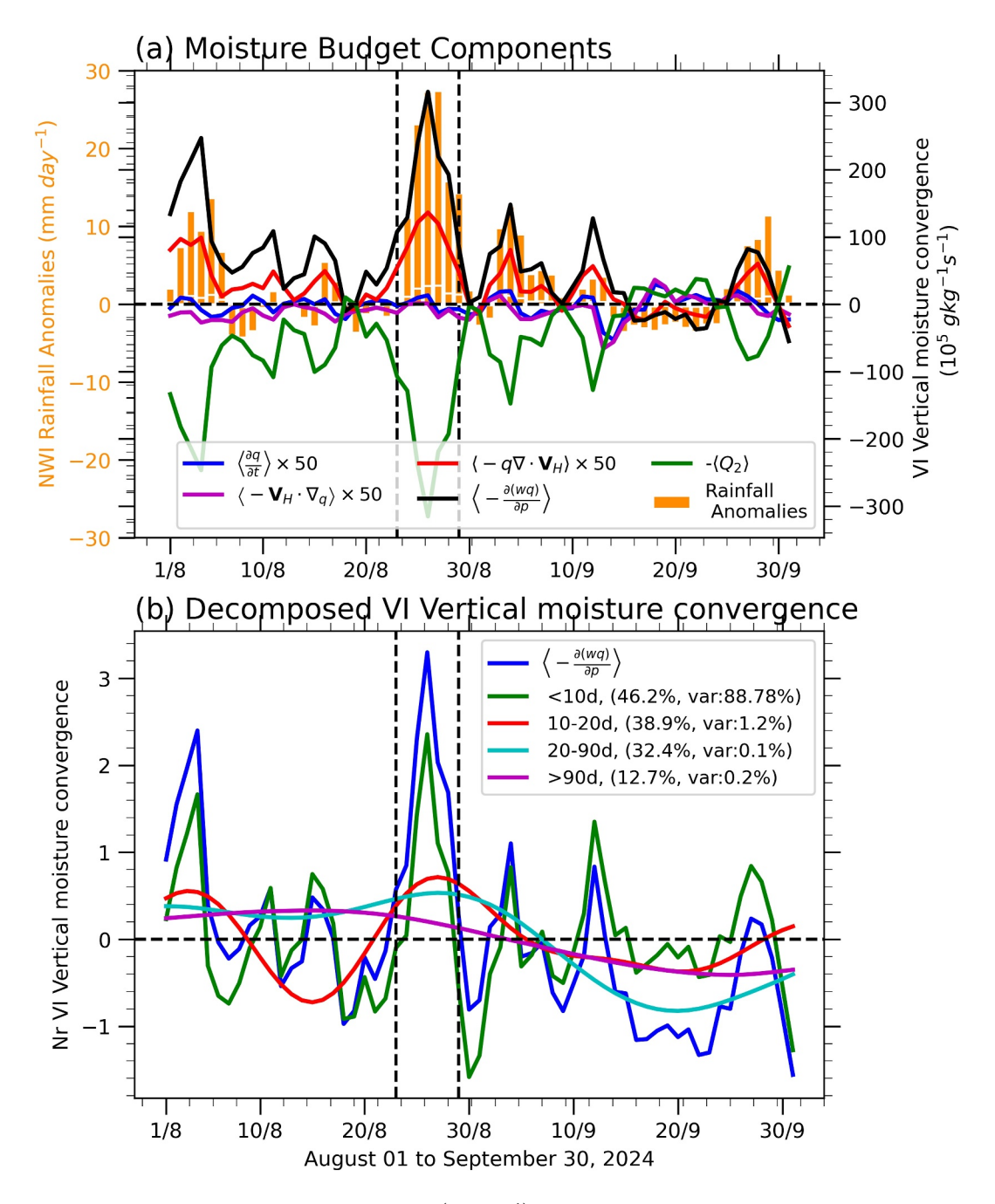


Figure 2. (a) Shows the temporal evolution of rainfall (mm day⁻¹) and column-integrated moisture budget terms over NWI derived from Equation 2. Orange colored bars represent rainfall anomalies (mm day⁻¹), while lines depict various moisture budget components: mean horizontal moisture advection (magenta), horizontal moisture convergence (red), vertical moisture convergence (black), total moisture convergence (blue), and moisture sink (green). (b) Decomposition of vertical moisture convergence into different time scales: synoptic (<10 days; green), quasi-biweekly (10–20 days; red), intraseasonal (20–90 days; cyan), and seasonal/interannual (>90 days; magenta), labels showing contribution and variance percentages of respective bands.

vertical structure becomes more disorganized while maintaining substantial intensity multiple smaller forcing centers develop, accompanied by a similarly fragmented rainfall pattern showing multiple peaks (50 mm day⁻¹ near 20°N and 30 mm day⁻¹ around 30°N), suggesting what Krishnamurthy (2019) describes as the "multimodal breakdown phase" where the initially coherent system begins fragmenting into smaller convective elements. The final phase (29–30 August) shows considerable weakening and restructuring of the forcing pattern. New positive

MAHENDRA ET AL. 9 of 29

21698996, 2025, 21, Downloaded from https://agupubs.onlinelibrary.wiley.com/doi/10.1029/2025JD044227 by Kieran Hunt - NICE, National Institute for Health and Care Excellence

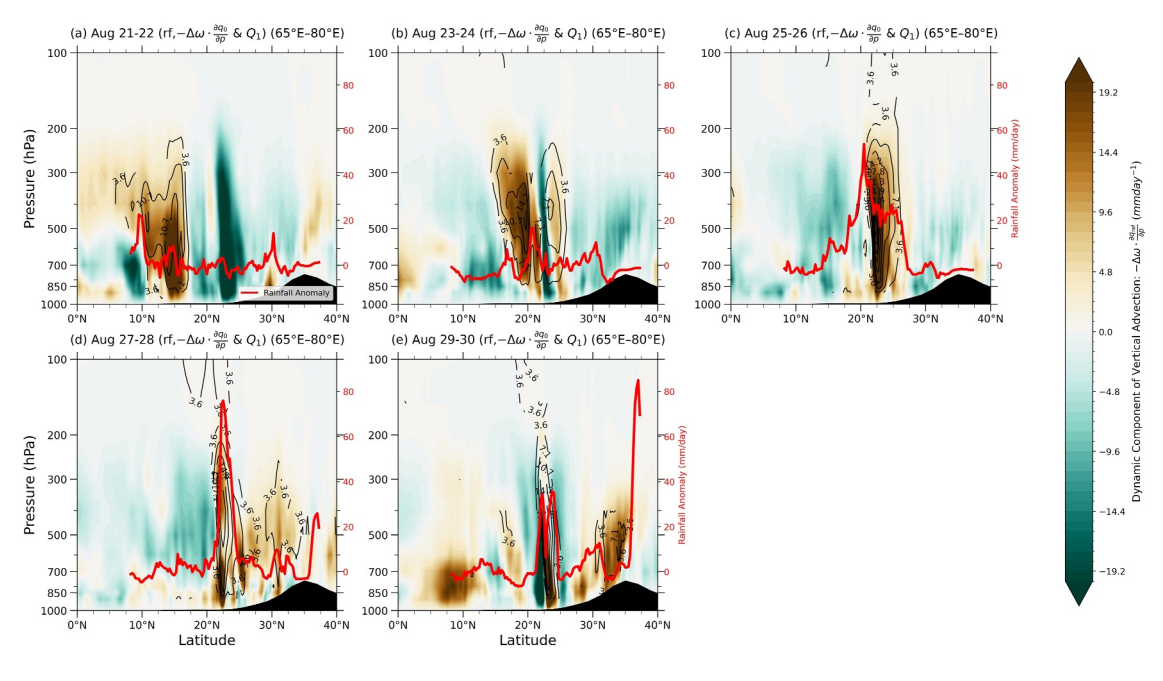


Figure 3. Latitude-pressure cross-sections (65°E-80°E) showing the dynamic component of vertical moisture advection (shaded, mm day⁻¹), diabatic heating rate Q₁ (contoured, K day⁻¹), and zonal mean rainfall anomalies (red line, mm day⁻¹, right axis) during August 2024. Panels represent consecutive 2-day periods: (a) 21–22 August, (b) 23–24 August, (c) 25–26 August, (d) 27–28 August, and (e) 29–30 August. The black shaded region at the bottom of each panel represents topography.

forcing centers develop at 30°N-35°N in the mid-troposphere, while lower-level forcing appears near 5°N, indicating the system's decay and energy redistribution (Figure 3e). This evolution is reflected in the rainfall anomalies which show an intense but narrowly confined peak (80 mm day⁻¹) centered at 35°N, while precipitation elsewhere diminishes. This evolution matches Parker et al. (2016) description of how synoptic-scale systems propagate and transform as they complete their lifecycle. The black shaded region at the bottom of each panel represents the Tibetan Plateau topography, which Hunt and Turner (2017) identified as a critical feature in modulating vertical motion during NWI precipitation events through mechanical lifting and thermal effects. The thermodynamic vertical moisture advection (see Figure S5 in Supporting Information S1) exhibits more diffuse patterns with weaker magnitudes, overall confirming dynamical process dominance during the

3.4. Moisture Back Trajectories 24, 25, and 26 August and Synoptic Conditions on 26 August 2024

Having examined the vertical structure of vertical moisture advection and diabatic heating, we now investigate the specific pathways through which moisture was transported to this extreme event and its association with background circulation. The 24 August trajectories (Figure 4c) show a recurving pattern from the Bay of Bengal with high specific humidity values (16-20 g kg⁻¹), establishing an "eastern moisture channel." These trajectories align with the 5,880 m geopotential height contour that extends eastward, creating a favorable channel for moisture transport along its southern periphery. On 25 August, trajectories (Figure 4b) display northward transport from CI with moderate humidity (10-16 g kg⁻¹), indicating continental moisture recycling through evapotranspiration. The 5,880-5,865 m geopotential height gradient over this region creates a pressure differential that facilitates this northward moisture advection. By 26 August, trajectories (Figure 4a) demonstrate the "western moisture conveyor" with curved paths from the Arabian Sea enhancing moisture uptake (14-18 g kg⁻¹). This westward shift corresponds with the 5,880-5,850 m geopotential height contours forming a trough-like pattern that channels moisture-laden air from the Arabian Sea toward NWI. This multisource moisture convergence aligns with the dynamic vertical moisture advection structures identified earlier and exemplifies the complex atmospheric dynamics described by Hunt et al. (2021). The predominant trajectories spanning from the Arabian Sea to the Bay of Bengal demonstrate a moisture acquisition process modulated by large-scale circulation patterns. The convergence around 20-25°N represents a critical zone of moisture accumulation, illustrated by the closely packed

MAHENDRA ET AL. 10 of 29

21698996, 2025, 21, Downloaded from https://agupubs.onlinelibrary.wiley.com/doi/10.1029/2025JD044227 by Kieran Hunt

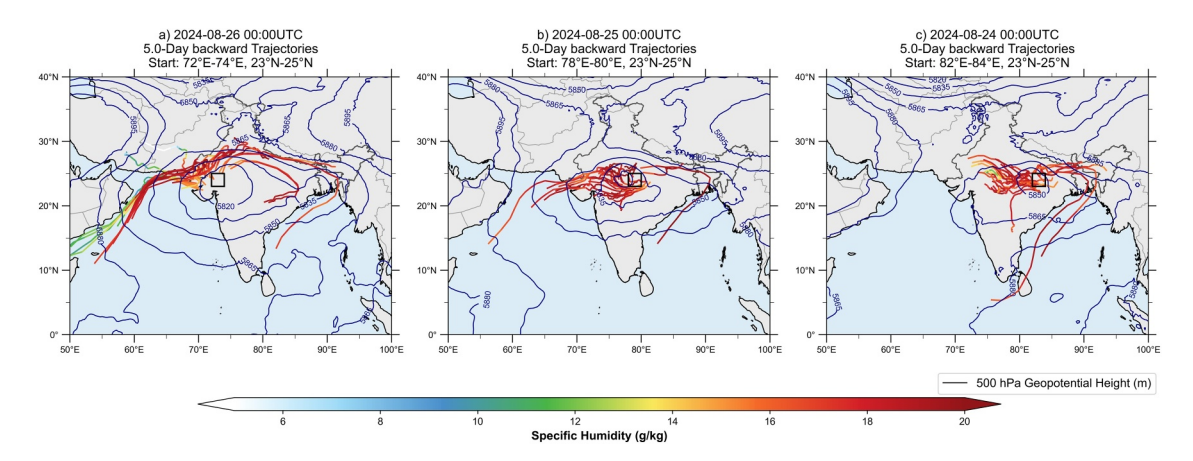


Figure 4. Five-day backward 800 hPa moisture trajectories initiated from three regions along the latitudes (23°N–25°N), along with 500 hPa geopotential height (m) contours at 00:00 UTC. (a) 26 August 2024 (starting longitude 72°E–74°E), (b) 25 August 2024 (starting longitude 78°E–80°E), and (c) 24 August 2024 (starting longitude 82°E–84°E). Trajectories are color-coded by specific humidity (g kg⁻¹) along their paths.

geopotential height contours, showing how air masses progressively gain moisture through nonlinear interactions with oceanic and terrestrial surfaces (Pathak et al., 2017).

The evolution of these patterns suggests that dynamic processes dominate during the intensification and mature phases, while thermodynamic contributions become relatively more important during the decay phase. The contrast between these components highlights the coupling mechanism that drives extreme precipitation events, with dynamic forcing serving as the primary driver and thermodynamic processes playing a supporting role in moisture redistribution. This moisture transport analysis prompted us to further investigate the synoptic conditions during the event.

Synoptic conditions on 26 August 2024, reveal a multilevel circulation system with an unusual path reminiscent of that described by Rajeevan et al. (2010). The vorticity path illustrated a complex moisture transport mechanism initiated by midlatitude dynamical forcing, with upper-level westerly winds (300 hPa) interacting with midtropospheric cyclonic circulation (500 hPa) B. Wang et al. (2021). Physically, the disturbance demonstrated a notable southeastward propagation, originating from the Caspian Sea region and penetrating toward the NWI through a precise alignment of atmospheric conditions in line with Hunt et al. (2021). The lower-level winds (850 hPa) exhibited exceptional moisture convergence, supported by unusually high 500-hPa relative humidity (70%–100%), much higher than is typical for a monsoon break Xavier et al. (2018). This mechanism aligns with Karmakar et al. (2022), Mahendra et al. (2024)'s hypothesis of midlatitude dynamical forcing capable of generating intense precipitation through a nuanced interaction of kinematic and thermodynamic processes. The vorticity centers, tracked across multiple pressure levels, demonstrated a complex rotational system where positive vorticity (>5 × 10^{-5} s⁻¹) facilitated vertical lifting and moisture redistribution, effectively overcoming the typical suppression mechanisms during the monsoon break. Fundamentally, this event exemplifies how synoptic-scale atmospheric configurations can generate localized extreme precipitation through intricate interactions between horizontal moisture transport, vertical atmospheric motion, and regional circulation patterns (Figure 5).

Given the critical role of midlatitude influence identified in our analysis, we next investigate the specific midlatitude dynamics and wave patterns that contributed to this exceptional event.

3.5. Global Temperature Anomalies and Mid-Tropospheric Baroclinic Instability Over the North Atlantic

Having established the synoptic-scale circulation patterns, we now examine the larger-scale thermal forcing that may have contributed to this event. The global SST anomalies for August 2024 display distinct regional warming patterns (Figure 6a). Strong positive SST anomalies (1–3°C) dominate the North Atlantic, particularly in midlatitude regions, reflecting accelerated warming in the Gulf Stream sector extension linked to Atlantic meridional overturning circulation (AMOC) weakening pattern (K.-Y. Li & Liu, 2025; Rahmstorf, 2024; Todd & Ren, 2023). The North Pacific, western Indian Ocean, and Arabian Sea also show notable warming (0.5–2°C), while equatorial Pacific conditions remain neutral. These patterns drive strong atmospheric responses: North Atlantic

MAHENDRA ET AL. 11 of 29

21698996, 2025, 21, Downloaded from https://agupubs.onlinelibrary.wiley.com/doi/10.1029/2025J044277 by Kiran Hunt - NICE, National Institute for Health and Care Excellence, Wiley Online Library on [07/11/2025]. See the Terms and Conditions

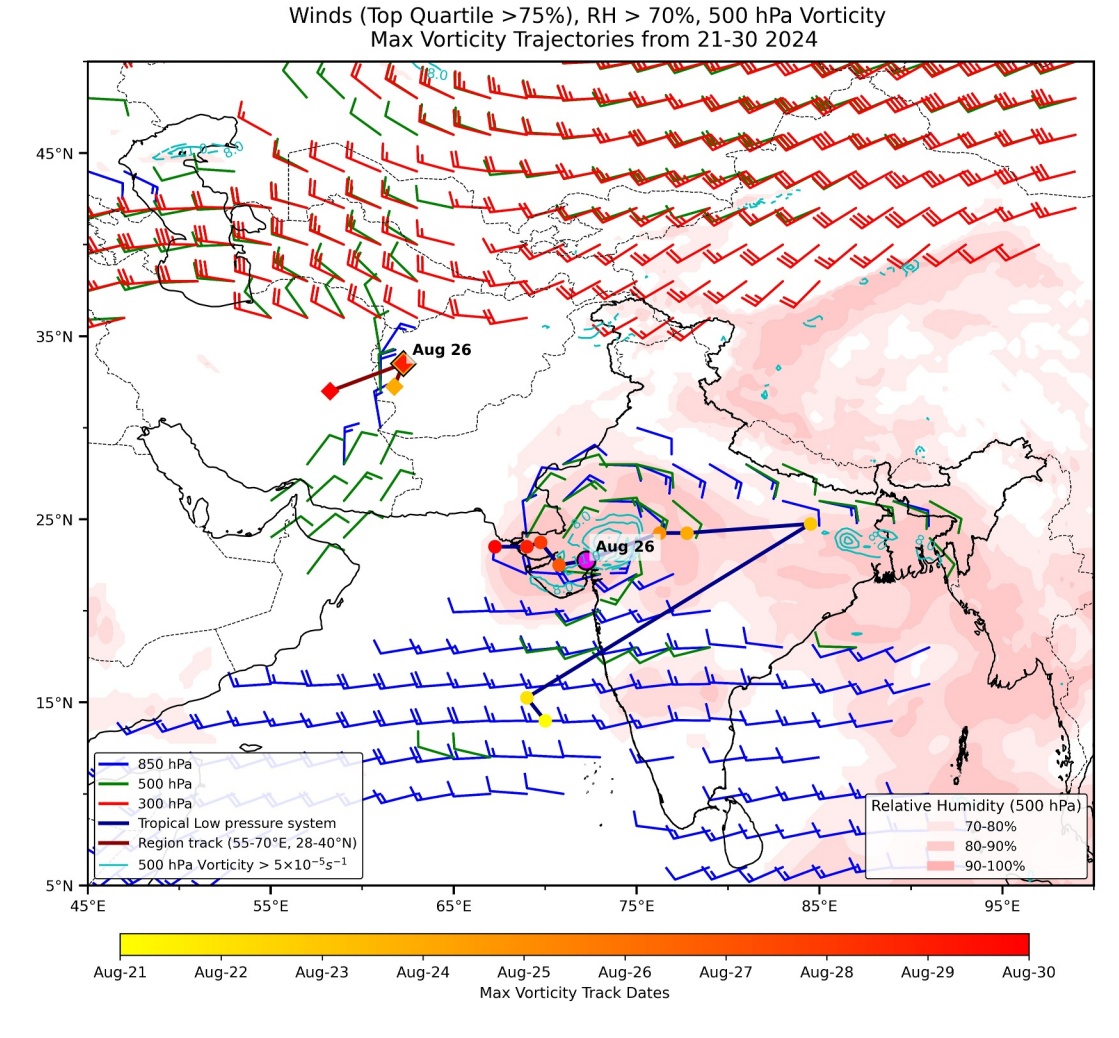


Figure 5. Synoptic conditions on 26 August 2024, showing upper-air circulation patterns over South and Central Asia. Wind barbs represent winds (m s⁻¹) exceeding the 75th percentile at three pressure levels: 850 hPa (blue), 500 hPa (green), and 300 hPa (red). Shaded areas indicate relative humidity at 500 hPa (70%–80%, 80%–90%, and 90%–100%). Cyan contours show regions of significant positive vorticity (>5 × 10^{-5} s⁻¹) at 500 hPa. Two 850 to 500 hPa levels averaged maximum vorticity trajectory tracks are displayed: the main Indian domain track (thick blue line with purple circle marking 26 August position) and a regional track (55–70°E, 28–40°N; brown line with orange diamond marking 26 August position), red dots along the tracks indicate daily positions from 21 to 30 August.

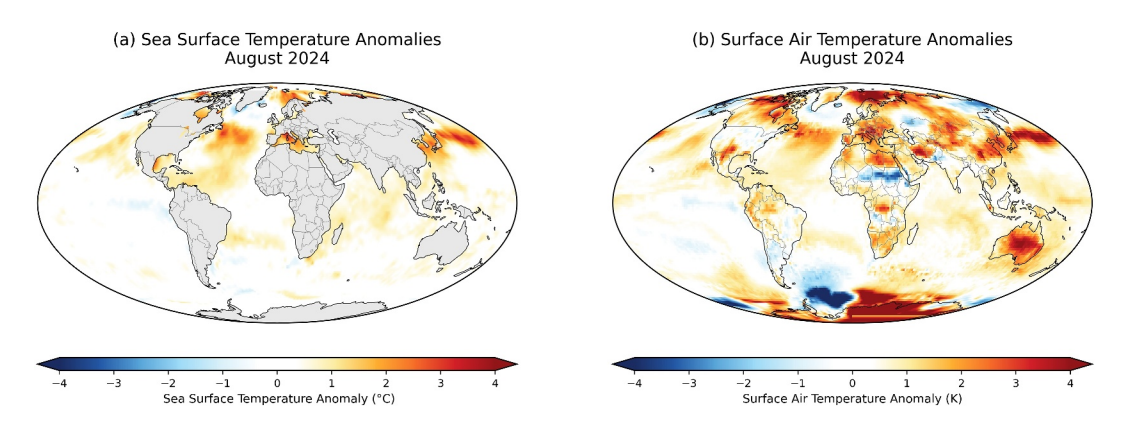


Figure 6. Global temperature anomalies during August 2024. (a) Sea surface temperature anomalies ($^{\circ}$ C). (b) Surface air temperature anomalies ($^{\kappa}$ C).

MAHENDRA ET AL. 12 of 29

warming enhances baroclinicity by amplifying meridional temperature gradients, which strengthens the upper-level jet through a strong thermal wind balance (Scaife et al., 2017; Shaw et al., 2016; O'Reilly et al., 2017; Rahmstorf et al., 2015). While Arabian Sea warming increases directly enhanced moisture transport toward NWI, providing crucial thermodynamic forcing for the extreme precipitation event (Xavier et al., 2018; Zhang & Delworth, 2005).

These SST patterns provide important context for understanding the midlatitude dynamics observed during this event. However, North Atlantic SST anomalies can modulate atmospheric baroclinicity through changes in the lower tropospheric temperature gradient (Figure 6a) (O'Reilly et al., 2017). Hence, the Gulf Stream temperature gradients are becoming critical for maintaining North Atlantic storm tracks and the associated westerly jet. Yin (2005) documented how increased greenhouse warming can intensify and shift the westerly jets poleward due to enhanced temperature gradients. Using climate model projections, this study showed that the increased meridional temperature gradient in the upper troposphere enhances baroclinicity and causes a strengthening of the westerly jet.

Complementary surface air temperature (SAT) anomalies for August 2024 reveal the regional thermal structure supporting this event. Figure 6b reveals SAT anomalies for August 2024. Intense warming (3 – 4K) dominates Northern Eurasia, particularly Russia and Mongolia, extending across the Middle East and Central Asia, while North America and Western Europe also exhibit significant positive anomalies. A distinctive thermal dipole appears between the Iran High region and NWI—strong warming over Iran contrasts with cooling over NWI, creating horizontal temperature gradients that reinforced the observed circulation pattern Ding and Wang (2005). This thermal dipole pattern directly corresponds to the dynamical forcing that sustained moisture advection from the Arabian Sea toward NWI throughout the event period (B. Li et al., 2023). Moreover, the hemispheric-scale warming pattern supports Francis and Vavrus (2012)'s hypothesis that amplified northern latitude warming creates persistent weather patterns through altered jet stream dynamics, highlighting the critical connection between regional temperature anomalies and the atmospheric circulation driving the extreme precipitation event.

3.6. Evolution of Baroclinic Instability and Energy Fluxes

Following our analysis of temperature anomalies, we now examine how these thermal patterns translated into dynamic instabilities and energy fluxes. The evolution of baroclinic instability, vertically integrated eddy kinetic energy flux, and vertically integrated northward heat flux (VINHF) (Figure 7) reveals critical atmospheric dynamics that modified the eddy-driven jet stream position and strength (Hartmann, 2015), characteristic of an amplified synoptic-scale flow pattern (H. Nakamura & Wallace, 1993). Time series analysis shows mid-tropospheric baroclinic instability (500 hPa EGR) averaging 0.67 day⁻¹ for the month, exceeding the climatological mean of 0.62 day⁻¹, while lower-tropospheric instability (850 hPa EGR) similarly surpassed normal conditions at 0.53 day⁻¹ compared to the typical 0.50 day⁻¹ (Figures 7a and 7b). A pronounced peak in 500 hPa EGR occurred between 13 and 17 August, reaching values above 0.8 day⁻¹ (1.34 σ), indicating significantly strong baroclinic instability as described by Hoskins and Hodges (2019), which is noted 7–10 days before the NWI rainfall event.

Spatial analysis over 14–20 August reveals intense baroclinic instability centered over the North Atlantic, with EGR values exceeding $1.0 \, \mathrm{day^{-1}}$. The vertically integrated eddy kinetic energy flux (red arrows) illustrates a coherent eastward-directed wave train originating from this region, with flux magnitudes exceeding $1.5 \times 10^6 \, \mathrm{W m^{-1} s^{-1}}$ in core regions (Figure 7c). This energy propagation follows the midlatitude waveguide. This pattern represents the atmospheric Rossby wave response to the enhanced baroclinic instability, showing strong energy propagation upstream over the North Atlantic and downstream over central Eurasia along the jet stream in a circumglobal teleconnection pattern similar to that identified by Krishnan and Sugi (2001).

In addition to this, VINHF quantifies the meridional transport of heat by these developing eddies (Figure 7d). The alternating bands of positive $(3-4\times10^6~\mathrm{W~m^{-1}~s^{-1}})$ and negative $(-3\times10^6~\mathrm{W~m^{-1}~s^{-1}})$ heat flux values demonstrate the wave-like nature of energy transport, with positive values indicating poleward heat transport where warm air moves northward and cold air southward—a signature of developing baroclinic waves as detailed by Orlanski and Chang (1993). This sequence represents a classic case of baroclinic energy conversion and propagation processes. The North Atlantic region's enhanced temperature gradients created ideal conditions for cyclogenesis through baroclinic instability. The resulting energy propagation established a hemispheric-scale teleconnection pattern across Eurasia, which seemingly began 7–10 days before the NWI rainfall event,

MAHENDRA ET AL. 13 of 29

21698996, 2025, 21, Downloaded from https://agupubs.onlinelibrary.wiley.com/doi/10.1029/2025JD044227 by Kieran Hunt - NICE, National Institute for Health and Care Excellence

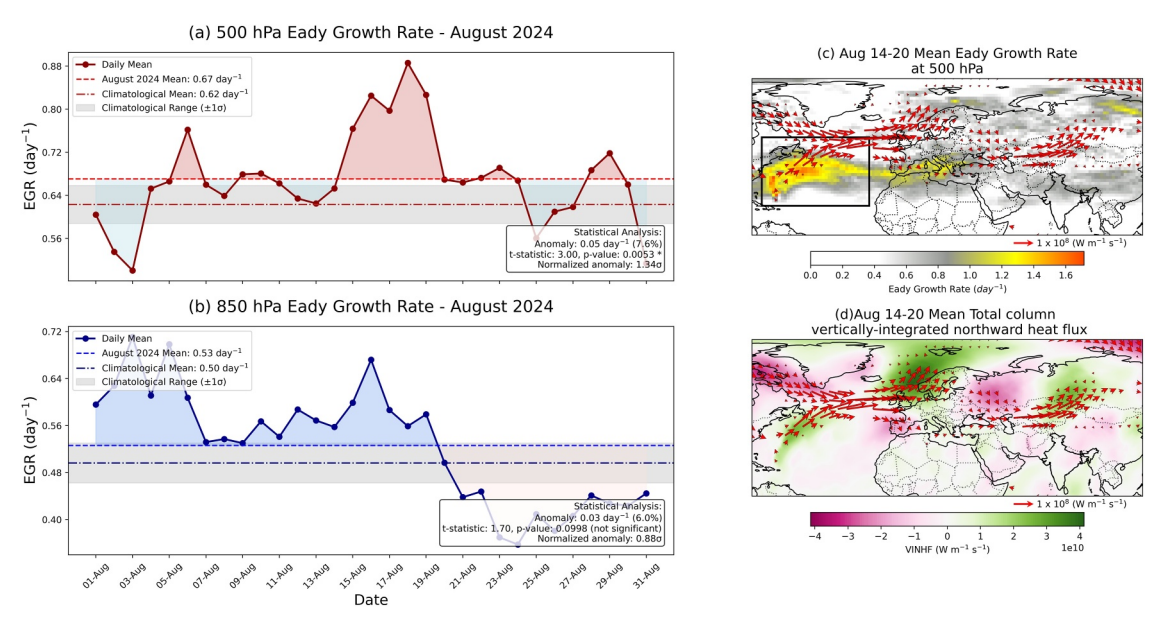


Figure 7. (a) Daily Eady growth rate (day⁻¹) over the black box indicates the North Atlantic region at 500 hPa showing daily values (maroon line), August 2024 mean (red dashed line), climatological mean (maroon dashed line), and climatological range (gray shading). (b) Daily EGR at 850 hPa with daily values (dark blue line), August 2024 mean (blue dashed line), climatological mean (dark blue dashed line), and climatological range (gray shading). Statistical significance of anomalies is indicated in the box. (c) Spatial distribution of mean Eady growth rate at 500 hPa for 14–20 August, 2024, with vertically integrated kinetic energy flux vectors (Wm⁻¹ s⁻¹). (d) Mean total column vertically integrated northward heat flux (Wm⁻¹ s⁻¹) for 14–20 August, 2024, with vertically integrated kinetic energy flux vectors (Wm⁻¹ s⁻¹).

aligning with teleconnection time scales between North Atlantic wave breaking and Asian monsoon precipitation anomalies identified by Ding and Wang (2007) and Martius et al. (2013).

3.7. Evolution of Upper Tropospheric Flow Patterns

We now examine how these dynamics manifested in the evolution of upper tropospheric flow patterns. Figure 8 illustrates this progression. Figure 8a shows the 21–22 August initial configuration with several important features: A well-defined midlatitude jet stream (black contours) with moderate amplification, wind speed maxima concentrated over the south of Greenland/eastern North Atlantic and central Eurasia, and early development of a European/Ural blocking pattern (northward bulge in contours) toward the Ural Mountain region around 20°–50°E (X. Chen et al., 2021). Wind vectors indicate predominantly zonal flow with initial perturbation. This pattern resembles the precursor wave configuration described by Branstator (2002) in his analysis of circumglobal teleconnection patterns. The strong geostrophic winds south of Greenland facilitated significant energy transfer along the westerly jet (Rossby, 2020; Takaya & Nakamura, 2001). The Ural block development signals the initial phase of what H. Nakamura and Fukamachi (2004) termed an "incipient blocking episode", which often precedes downstream wave amplification.

Figure 8b depicts the 23–24 August period when the amplification of the Ural block strengthens and expands eastward as a pronounced trough develops over western Asia (60° E). Wind speed maxima intensify, with values exceeding 100 m s^{-1} (red shading). Flow patterns show an increased meridional component. This intensification phase demonstrates the "downstream development" mechanism articulated by Chang (2005), where perturbation energy propagates eastward along the waveguide. The strengthening trough over western Asia matches the "RWB" pattern documented by Martius et al. (2013), which plays a crucial role in facilitating downstream momentum transport toward South Asia.

In Figure 8c during 25–26 August, the circulation reaches peak intensity with formation of a closed anticyclonic circulation over the Europe/Ural Mountain region, a deep trough over the Caspian Sea region with cyclonic curvature, and intensification of the jet streak (dark red) over Central Asia exceeding speeds of 120 m s⁻¹. The enhanced meridional flow creates this pronounced wave train pattern. This structure exemplifies the "high-amplitude wave pattern" that Krishnan et al. (2009) linked to extreme precipitation events in South Asia. The jet

MAHENDRA ET AL. 14 of 29

21698996, 2025, 21, Downloaded from https://agupubs.onlinelibrary.wiley.com/doi/10.1029/2025JD044227 by Kieran Hunt - NICE, National Institute

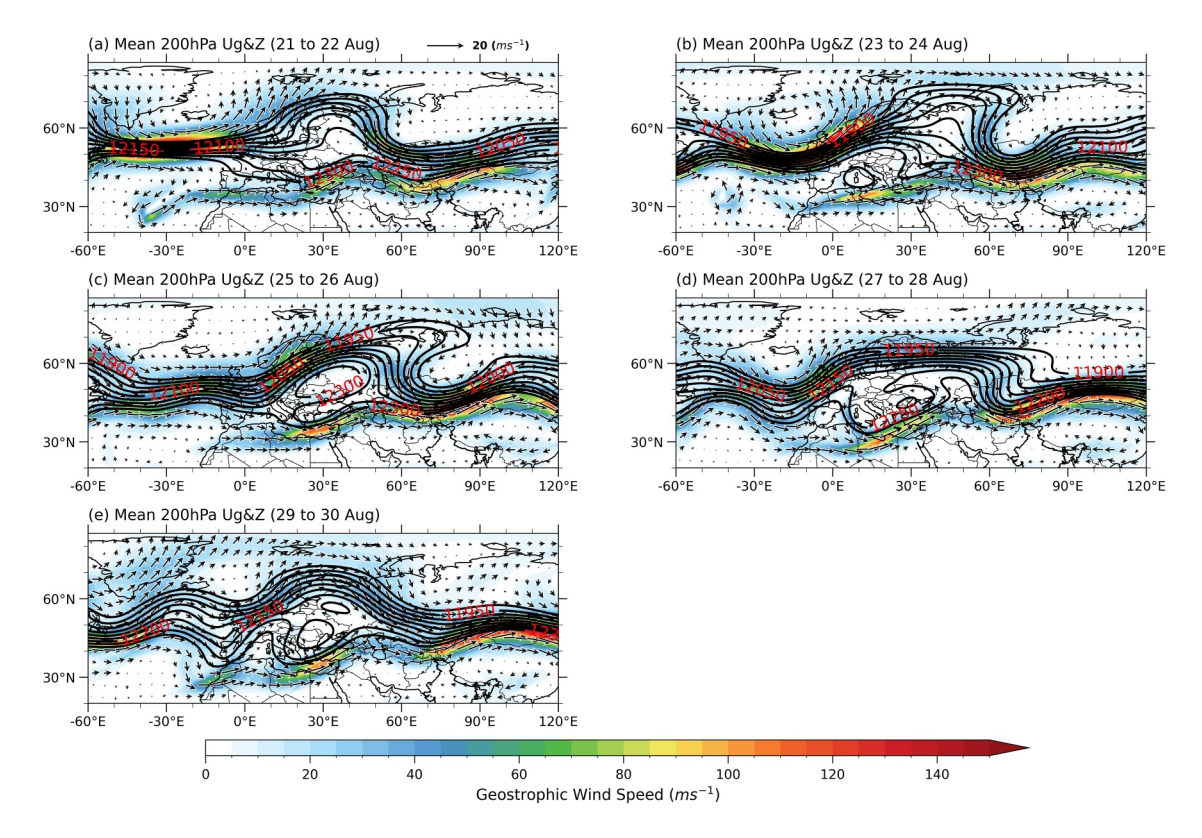


Figure 8. Evolution of upper-level circulation patterns showing 200-hPa geopotential height (contours, *m*), wind vectors (arrows, m s⁻¹), and geostrophic wind speed (color shading, m s⁻¹) for five consecutive 2–day periods: (a) 21–22 August, (b) 23–24 August, (c) 25–26 August, (d) 27–28 August, and (e) 29–30 August, 2024.

streak positioned north of the Tibetan Plateau creates divergence in its right entrance region, directly affecting NWI through what Uccellini and Johnson (1979) identified as jet-induced secondary circulations.

Figure 8d shows the 27–28 August persistent phase where the system maintains intensity with subtle changes. The Ural block begins slight retrogression and the Central Asian jet streak reaches maximum intensity. The wave pattern shows signs of quasi-stationarity. This persistence phase matches Woollings et al. (2018) findings on how blocking patterns can maintain anomalous circulation features for extended periods. The "11,900 m" contour indicates the exceptional geopotential height associated with this intense circulation anomaly.

The last panel, Figure 8e, presents the 29–30 August final stage showing circulation evolution with the weakening of the Ural blocking pattern, eastward shift of the main jet streak, reduced amplitude of the wave pattern, and reorganization of the flow toward more zonal orientation. This sequence of flow pattern resembles the typical life cycle of Rossby wave packets described by Glatt et al. (2011), where wave energy ultimately propagates out of the region. In summary, the strong jet streak north of the Tibetan Plateau, led by the blocking signature over the Ural Mountain region and enhanced meridionality along the Eurasian corridor, created conditions favorable for extreme precipitation over NWI. This persistent pattern exemplifies the "quasi-resonant amplification" mechanism proposed by Mann et al. (2017) to explain extreme weather events associated with amplified quasi-stationary waves.

3.8. Process-Level Rossby Wave Diagnostics, LWA Framework

The LWA framework (C. S. Y. Huang & Nakamura, 2016) provides quantitative insights about Rossby wave dynamics, which is observed previously in Figure 8, emphasizing initial wave amplification over the North Atlantic and propagation characteristics. It is worth noting that the key process involves the anchoring of the NWI low-pressure system by midlatitude upper-level circulation, resulting in prolonged heavy precipitation. The diagnostics of upper-tropospheric dynamics during 21–30 August, 2024, through QGPV, LWA, and wave activity flux (WAF) capture the peak phase of wave development on 25 August (Figure 9a). The synoptic map displays multiple diagnostic fields with QGPV distribution shaded (positive/cyclonic, negative/anticyclonic). Streamlines

MAHENDRA ET AL. 15 of 29

21698996, 2025, 21, Downloaded from https://agupubs.onlinelibrary.wiley.com/doi/10.1029/2025/D044227 by Kieran Hunt - NICE, National Institute for Health and Care Excellence, Wiley Online Library on [07/1/12025]. See the Terms and Conditions (https://agupubs.onlinelibrary.wiley.com/doi/10.1029/2025/D044227 by Kieran Hunt - NICE, National Institute for Health and Care Excellence, Wiley Online Library on [07/1/12025]. See the Terms and Conditions (https://agupubs.onlinelibrary.wiley.com/doi/10.1029/2025/D044227 by Kieran Hunt - NICE, National Institute for Health and Care Excellence, Wiley Online Library on [07/1/12025]. See the Terms and Conditions (https://agupubs.onlinelibrary.wiley.com/doi/10.1029/2025/D044227 by Kieran Hunt - NICE, National Institute for Health and Care Excellence, Wiley Online Library on [07/1/12025]. See the Terms and Conditions (https://agupubs.onlinelibrary.wiley.com/doi/10.1029/2025/D044227 by Kieran Hunt - NICE, National Institute for Health and Care Excellence, Wiley Online Library.

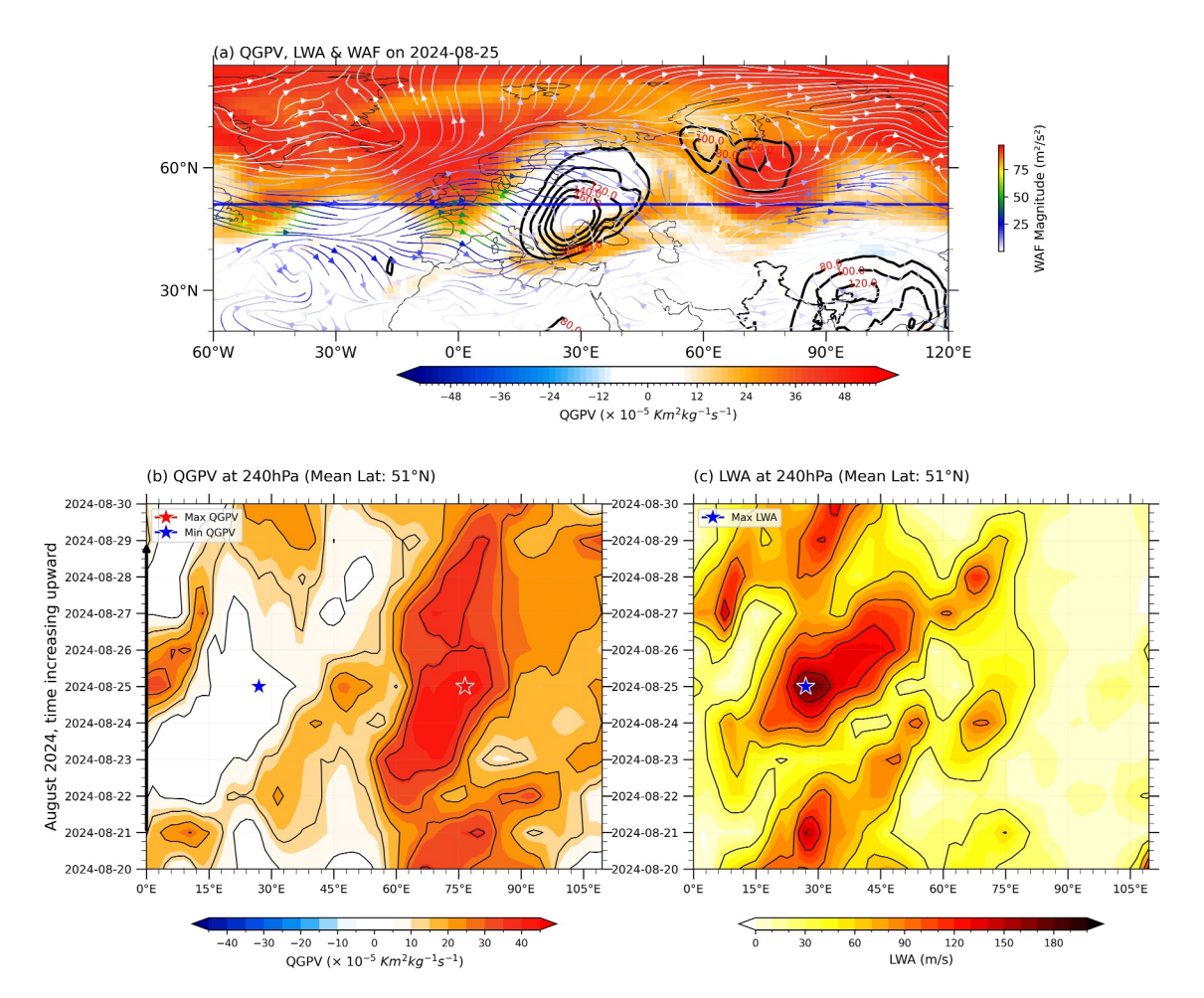


Figure 9. (a) Horizontal distribution of quasi-geostrophic potential vorticity (QGPV, shaded, $\times 10^{-5}$ K m²kg⁻¹s⁻¹) with wave activity flux (WAF, blue vectors, magnitude in m² s⁻²) and streamlines (white) at 200 hPa on 25 August 2024. Black contours represent local wave activity (LWA, m s⁻¹). (b) Hovmöller diagram of QGPV at 240 hPa along 51°N showing the eastward propagation of vorticity features during 20–30 August, 2024. Stars mark the locations of maximum (white) and minimum (blue) QGPV values. (c) Corresponding Hovmöller diagram of LWA at 240 hPa along 51°N with the location of maximum LWA marked by a blue star.

show the instantaneous flow pattern, while black contours display the LWA field intensity, highlighting regions of wave amplification. WAF vectors indicate the energy propagation magnitude and direction.

The pattern reveals several critical features: a strong positive QGPV over the Caspian Sea region (60°E) indicating intense cyclonic eddy development; a pronounced negative QGPV area (30°E) representing the European blocking high with enhanced LWA values (black contours exceeding 120 m s⁻¹) over Europe, signifying exceptional wave amplitude; and WAF vectors showing eastward energy propagation from the North Atlantic-European sector toward Asia. This configuration exemplifies what N. Nakamura and Huang (2018) termed "finite-amplitude wave packet dynamics," where blocking patterns and downstream cyclogenesis occur simultaneously as part of a wave train. The strong WAF magnitude (yellow to red arrows) aligns with Takaya and Nakamura (2001) findings on how blocking episodes enhance downstream energy propagation through waveguide dynamics. This energy propagation followed classical WAF (see Figure S8 in Supporting Information S1) principles (Rossby, 2020; Takaya & Nakamura, 2001), where the interaction between tropospheric and stratospheric potential vorticity anomalies play a crucial role in block intensification. The subsequent downstream development affected Western and Central Europe through what appears to be a downstream development process involving RWB (Pelly & Hoskins, 2003). Weakened meridional PV gradients reduced the basic-state westerly flow. Strong nonlinear interactions maintained the block against dissipation until 26 August (Luo et al., 2018). Particularly, the weak meridional PV gradient and enhanced nonlinearity created conditions that supported a long-lasting blocking pattern (Figures 8b-8d), consistent with the findings of N. Nakamura and Huang (2018), Yan et al. (2024) on block persistence mechanisms.

MAHENDRA ET AL. 16 of 29

Figure 9b QGPV Hovmöller diagram tracks QGPV evolution along 51°N at 240 hPa throughout the event period. Warm colors (red/orange) indicate positive QGPV (cyclonic circulation), while white/light colors represent near-zero QGPV. A blue star marks minimum QGPV (30°E on 25 August), identifying the core of the blocking high, while a red star indicates maximum QGPV (75°E on 25 August), directly corresponding to the Caspian Sea downstream cyclonic development. The diagram reveals a clear eastward-propagating wave pattern with alternating positive/negative QGPV anomalies. The blocking high (negative QGPV near 30°E) persisted for several days, while downstream development shows positive QGPV propagating toward Central Asia around 22–26 August. This progression matches the "PV wave-breaking and downstream development" paradigm described by Martius et al. (2008), where blocking events trigger downstream cyclogenesis through PV advection patterns.

However, LWA Hovmöller diagram (240 hPa, 51°N) in Figure 9c shows LWA magnitude evolution along the same latitude band. Warm colors (red/orange) indicate high LWA values representing strong wave amplification, with a blue star marking maximum LWA (30°E on 25 August), coinciding with the European blocking pattern. Multiple high-LWA regions appear in a diagonal pattern, indicating eastward propagation. The pronounced LWA maximum centered at 30°E around 25 August (exceeding 150 m s⁻¹) confirms exceptional wave amplification associated with the European blocking high. Secondary maxima appear downstream around 75°E and 15°E, representing the associated trough and upstream ridge, respectively. This pattern demonstrates what X. Chen et al. (2018) called "amplified stationary wave configuration", where wave activity concentrates in specific longitudes, enhancing meridional flow patterns. The temporal evolution shows LWA peaking first at 30°E (24–25 August) before intensifying downstream, confirming the causal relationship between the European blocking and the subsequent development over Asia. This sequence aligns with Kornhuber et al. (2017) findings on how amplified quasi-stationary waves can trigger extreme weather events through persistent circulation.

This analysis is complemented by the WAF evolution (see the Figures S8–S10 in Supporting Information S1) and supports these findings, showing a clear progression of energy propagation from the North Atlantic to Asia. Initially (21-22 August), moderate flux with zonal alignment over the North Atlantic represented the incipient wave packet development Takaya and Nakamura (2001). This intensified into organized propagation along the jet path by 23-24 August, exemplifying the "downstream development" mechanism Chang and Yu (1999). Peak organization occurred during 25-26 August, displaying the classic "great circle route" of Rossby wave propagation (Hoskins & Ambrizzi, 1993), with energy directed toward Central Asia. After maintaining strong flux across the North Atlantic-Eurasian sector during 27-28 August, the wave train structure weakened by 29-30 August, completing the typical lifecycle of Rossby wave packets Glatt and Wirth (2014). Moreover, LWA budget analysis (Figure S9 in Supporting Information S1) also shows strengthening wave organization and intensified meridional transport, with peak meridional heat flux during 23-26 August confirming poleward warm air transport associated with the developing ridge-trough pattern. Wave-mean flow interactions actively accelerated the zonal flow over Northern Eurasia during 25-28 August, while nonlinear wave-wave interactions produced characteristic dipole patterns of blocking dynamics. This evolution aligns with N. Nakamura and Huang (2018) "traffic jam" theory, where LWA accumulated upstream of the European/Ural block, while energy propagated downstream toward Asia, accelerating the subtropical jet that established the initial forcing for the jet streak-induced circulation that would steer the tropical system into the region and can trigger NWI's extreme rainfall (Figure S10 in Supporting Information S1).

3.9. Eddy Energetics Evolution and NWI Low-Pressure System Anchoring Mechanism

We now examine the energetics that powered these atmospheric circulation patterns. The upper tropospheric eddy energetics analysis at 200 hPa during 21–30 August. During 21–22 August, emerging wave train features showed eddy kinetic energy (EKE) concentrations over the North Atlantic, Western Europe, and Central Asia, with positive barotropic energy conversion (BEC) regions where mean flow energy was transferred to eddies (Figure 10a). This organized wave train began to develop with alternating EKE maxima aligned along the waveguide as detailed above. The positive BEC regions over the eastern North Atlantic represented "energy generation regions", where baroclinic disturbances extracted energy from the mean flow, aligning with Chang et al. (2002) findings on localized energy sources preceding downstream propagation. As the pattern evolved through the development during 23–24 August, EKE maxima intensified over Europe and western Asia, with a pronounced dipole structure of BEC emerging (Figure 10b). Positive conversion appeared on the upstream sides of EKE maxima and negative conversion on the downstream sides, while the wave train structure became more coherent with centers roughly 60°E longitude apart. This pattern exemplified the "downstream development"

MAHENDRA ET AL. 17 of 29

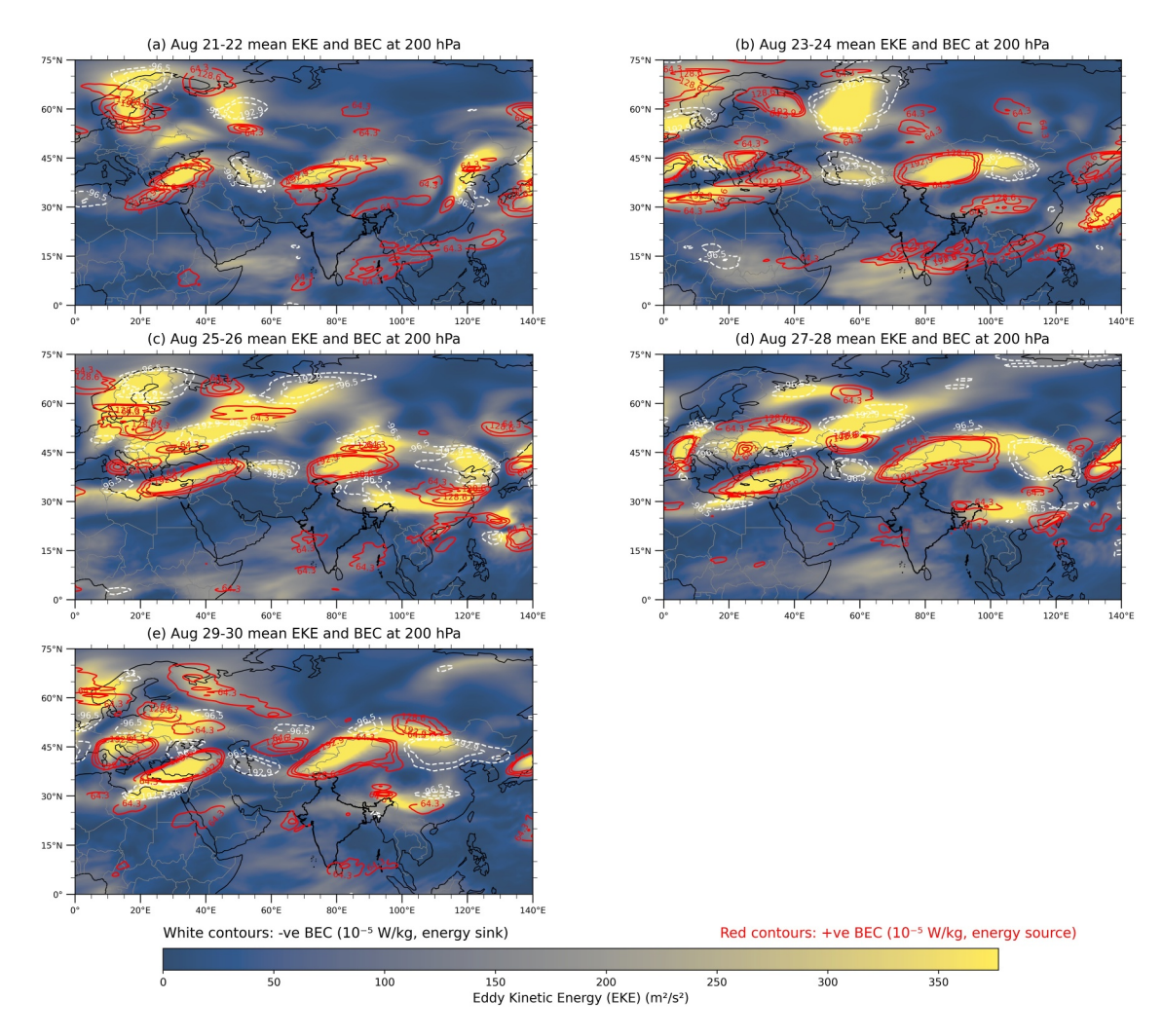


Figure 10. (a–e) Shows evolution of each plot 2-day means of eddy kinetic energy (EKE, color-shaded from 0 to 350 m² s⁻²) and barotropic energy conversion (BEC, red and white contours) across the Asian-Pacific region from 21 to 30 August, 2024. White contours represent negative BEC (10^{-3} W kg⁻¹, energy sink), while red contours indicate positive BEC (10^{-3} W kg⁻¹, energy source).

mechanism (Orlanski & Sheldon, 1995), where energy dispersion occurred through ageostrophic geopotential fluxes (Figure S8 in Supporting Information S1). The alternating positive/negative BEC pattern surrounding each EKE maximum demonstrated the energy propagation mechanism (Mak & Cai, 1989). Concentrated energy drove jet streak dynamics and can steer the low-pressure system northwestward. This, coupled with the upper-level trough and abundant moisture through the monsoon LLJ, triggered severe rainfall and aggravated existing conditions (Dong et al., 2018).

During 25–26 August, maximum EKE values (>300 m² s⁻²) appeared over Northern Europe and Central Asia, with an enhanced zonal band of EKE connecting these centers along 45°–60°N (Figure 10c). Positive BEC regions intensified on the upstream flanks of major EKE centers, and a clear Wave-5 pattern emerged in the Northern Hemisphere (figure not shown). This peak energy phase corresponded to maximum jet streak strength, maintaining the NWI system quasi-stationary while the LLJ sustained deep convection through continuous moisture transport, resulting in prolonged heavy rainfall (Xavier et al., 2018). This configuration represented "maximum barotropic amplification", where the wave pattern achieved optimal phasing relative to the background flow. As the event continued through its sustained phase (27–28 August), the wave pattern maintained intensity but showed slight eastward progression. EKE maxima over the North Atlantic redeveloped while Central Asian centers persisted, with BEC patterns indicating continued energy extraction from the mean flow (Figure 10d). Enhanced meridional elongation of EKE centers suggested increased wave amplification. This

MAHENDRA ET AL. 18 of 29

persistent energy configuration maintained the jet streak-induced anchoring mechanism and LLJ moisture transport, explaining the prolonged precipitation event. In the 29–30 August period, overall EKE intensity diminished, particularly over Central and Eastern Asia, as the wave pattern showed signs of fragmentation with a less coherent structure. BEC patterns weakened, indicating reduced energy exchange between eddies and mean flow, while new EKE development began over the North Atlantic, suggesting a regime transition (Figure 10e). The weakening EKE directly corresponded to the breakdown of jet streak dynamics and LLJ moisture transport, the extreme precipitation event. This evolution followed the typical lifecycle of Rossby wave packets described by Chang (2000), where wave energy ultimately disperses after peak intensity.

Having established the horizontal energy propagation mechanisms, we will next examine the vertical coupling of the extratropical-tropical interaction that connected these upper-level dynamics to the surface precipitation extremes.

3.10. Vertical Structure and Coupling in Mid-Latitude and Tropical Interactions

The left column (Figures 11a-11e) displays latitude-height cross-sections along the 65°E - 80°E longitudinal band, revealing the evolution of meridional mass overturning circulation. During 21–22 August (Figure 11a), a typical monsoon pattern existed with a weak upward motion along the western coast of India near 15°N. This corresponds to moderate vertical moisture advection as noted by Ramaswamy (1962). The upper-level westerly jet north of the Tibetan Plateau was initially weak. By 23-24 August (Figure 11b), enhanced upward motion developed around 20°N concurrent with the strengthening of the upper-level jet. The most significant transformation occurred during 25-26 August (Figure 11c), when an intensified vertical circulation cell formed with robust ascending motion between 15° and 25°N, coupled with a significantly strengthened upper-level jet deepened up to 400 hPa. Figures 11c and 11d highlight the Northern Hemispheric dynamic interaction between local Hadley and local Ferrel cells interactions. At approximately 30°N, we observe the boundary between the monsoon cross-equatorial cell and thermally direct local Hadley cell inline with Joseph et al. (2024) (equator to $\sim 30^{\circ}$ N) along with the thermally indirect local Ferrel cell ($\sim 30-60^{\circ}$ N). This transition zone creates enhanced secondary vertical circulation (Uccellini & Johnson, 1979) that facilitates energy exchange between tropical and midlatitude systems (Webster et al., 1999). This interaction between the cells manifested and steered the moisture from the monsoon core region to NWI regions dominated by the local Hadley circulation influenced by the local Ferrel cell Figures 11m and 11n during 25–28 August.

This configuration represents what Ramaswamy (1962) termed the "monsoon-midlatitude interaction cell," where enhanced upper-level divergence drives anomalous vertical motion that overrides typical monsoon break conditions through jet-induced secondary circulations. The middle column (Figures 11f-11j) illustrates ageostropic wind difference between 200 minus 500 hPa vectors and relative humidity fields (RH>80%), capturing the evolution of moisture advection patterns. Initially (Figure 11f), limited high-humidity regions existed over NWI with strong moisture over the monsoon core region (CI). As the event progressed (Figures 11g and 11h), a pronounced moisture convergence pattern developed with strengthening northward flow adjacent to southward flow, creating what Vellore et al. (2016) described as a "moisture convergence corridor." During the peak phase around 25-26 August (Figure 11h), high-humidity areas expanded significantly over NWI, providing essential moisture for sustained precipitation despite the monsoon break conditions. This pattern aligns with above findings that midlatitude disturbances can enhance moisture convergence through alterations to regional circulation patterns. Figures 11i and 11j show the gradual weakening of this moisture convergence pattern in the latter stages of the event. The right column (Figures 11k-11o) depicts rainfall distribution and VIMFT vectors. Initially (Figure 11k), minimal precipitation was observed across the country as a result of monsoon break conditions, characterized by a northward shift of the monsoon trough and reduced rainfall over CI (Gadgil & Joseph, 2003; Rajeevan et al., 2010). During break periods, weakened low-level circulation leads to suppressed convection over the core monsoon zone. By 23-24 August (Figure 111), rainfall began increasing and low-level circulations strengthened, playing a crucial role in heavy precipitation development (Xavier et al., 2018). This culminated in concentrated heavy precipitation over NWI during 25-26 August (Figure 11m), with rainfall rates exceeding 100 mm day⁻¹. The VIMFT vectors reveal how moisture convergence patterns aligned precisely with rainfall distribution, demonstrating what Houze et al. (2017) termed "dynamically forced precipitation." The converging moisture transport vectors and strengthened low-level circulation in Figure 11m indicate that these circulations contributed significantly to developing the low-pressure system (Vishnu et al., 2016), with rainfall resulting

MAHENDRA ET AL. 19 of 29

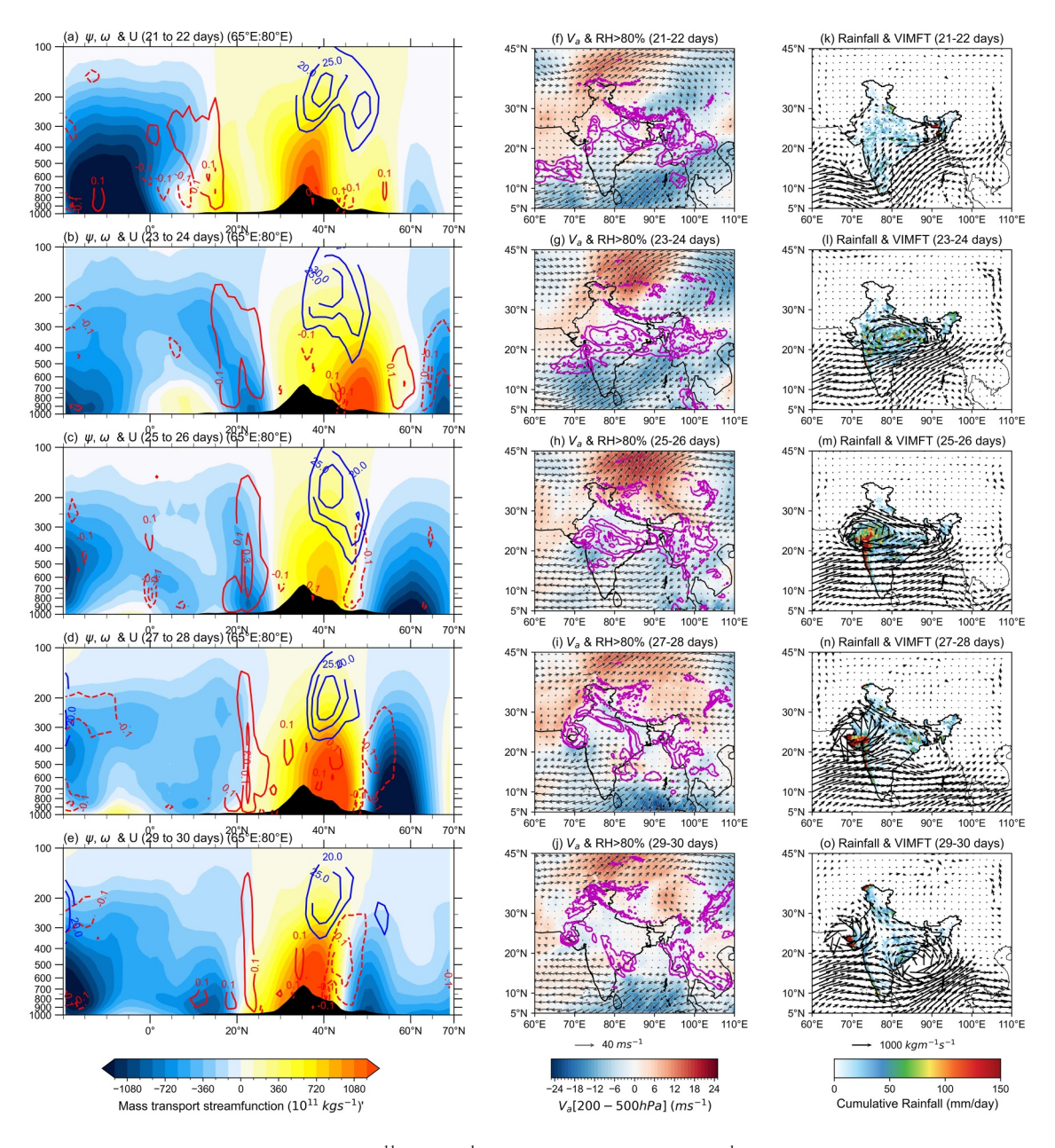


Figure 11. The left panels (a–e) display the stream function $(10^{11} \times kg \ s^{-1}$, shaded), vertical velocity (m s⁻¹, red contour lines; positive upward), and zonal wind (m s⁻¹, blue contour lines), averaged over the longitudinal band 65°E–80°E. The middle panels (f–j) present the meridional ageostrophic wind difference between 200 and 500 hPa (m s⁻¹, shaded), with vectors representing the ageostrophic wind field (m s⁻¹). Magenta contours highlight areas with relative humidity exceeding 80%, emphasizing regions of significant moisture content. The right panels (k–o) show cumulative rainfall (mm day⁻¹, shaded) and vertically integrated moisture flux transport (kg m⁻¹ s⁻¹, vectors). Each panel corresponds to 2-day mean fields, progressing sequentially from 21–22 August to 29–30 August, capturing the temporal evolution of atmospheric processes contributing to rainfall and circulation during this period.

primarily from large-scale forced ascent rather than local convective instability. By 29–30 August (Figure 11o), the moisture transport pattern had substantially weakened and rainfall diminished.

The six-hourly evolution of vorticity, zonal wind, and equivalent potential temperature (θ_e) was examined to further investigate the detailed coupling mechanisms between tropical and midlatitude systems. This analysis deepens our understanding of the vertical interactions between upper-level atmospheric dynamics and surface precipitation patterns.

MAHENDRA ET AL. 20 of 29

21698996, 2025, 21, Downloaded from https://agupubs.onlinelibrary.wiley.com/doi/10.10929025ID044227 by Kieran Hunt - NICE, National Institute for Health and Care Excellence, Wiley Online Library on [07/11/2025].

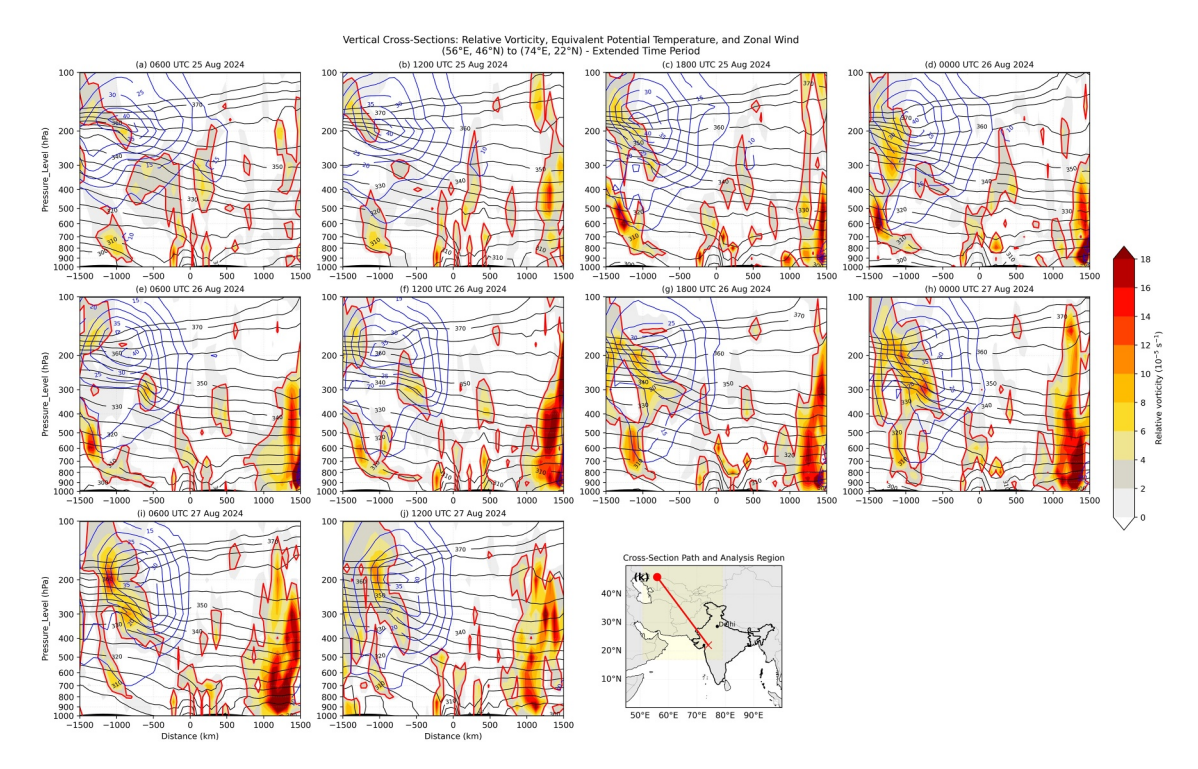


Figure 12. Vertical cross-sections of relative vorticity, equivalent potential temperature, and zonal wind for the extended region 55° – 74° E, 46° – 22° N during the 25 to 27 August, with a 15-degree buffer zone surrounding the core analysis cross-section region. (a–j) Each panel represents a six-hourly synoptic snapshot, spanning pressure levels from 1,000 to 100 hPa. Color shading indicates relative vorticity intensity, ranging from 0 to 18 s^{-1} (color scale), with black contour lines representing equivalent potential temperature and blue contours zonal wind. The (k) illustrates the precise cross-section path (red colored line) and analysis region over NWI (light yellowish shaded).

3.11. Vorticity Evolution Analysis

Figure 12 shows the sequence of vertical cross-section plots reveals the detailed evolution of atmospheric dynamics during 25–27 August, 2024. Initially, at 0600 UTC 25 August, the atmosphere exhibited a disorganized pattern with scattered vorticity patches primarily in the middle troposphere (400–700 hPa), while θ_e contours indicated a relatively stable environment with moderate thermal gradients. Zonal winds were relatively weak throughout most of the domain, with stronger winds confined to the upper levels where the blue contours represent the upper-level jet around 200 hPa in the northern portion of the cross-section. This represented the predevelopment stage with weak vertical coherence in vorticity, typical of monsoon environments before cyclogenesis as described by Goswami and Xavier (2005).

Six hours later, vorticity maxima began consolidating with stronger values (\sim 8–10 \times 10⁻⁵ s⁻¹) appearing at multiple levels, and a nascent vorticity column developed around the 500-km position. The zonal wind structure began showing more organization with the upper-level jet maintaining its position, with increased vertical wind shear beneath the jet. This initial vorticity organization was consistent with the "marsupial paradigm" described by Dunkerton et al. (2009), where protected regions of cyclonic vorticity begin to organize within larger-scale flow. By 1800 UTC 25 August, further intensification of vorticity structures became evident, particularly at lower levels (700–900 hPa), while the θ_e contours showed increased thermal gradients near areas of vorticity maxima, indicating frontogenetic processes. The zonal wind pattern showed increasing organization with more defined vertical variations, influenced by the developing baroclinicity through thermal wind relationships as described by Hoskins et al. (1985).

A significant transformation occurred by 0000 UTC 26 August, when a substantial vorticity maximum developed in the eastern portion at lower levels (700–1,000 hPa), which is the region of NWI, with values exceeding 12×10^{-5} s⁻¹. A significant change in the zonal wind pattern emerged as the developing system began to modify the background zonal flow, particularly at lower and midlevels, while the upper-level jet remained strong with peak winds around 30 m s⁻¹. Through 0600 UTC 26 August, continued organization maintained the eastern

MAHENDRA ET AL. 21 of 29

vorticity maximum, while new development appeared at 300–500 hPa around the 500-km position, with zonal wind structure evolving with maintained upper-level jet strength but increasing perturbations in the midlevels. These developments matched findings from Raymond et al. (2011) on the importance of midlevel vorticity in tropical cyclogenesis. Dramatic intensification became evident by 1200 UTC 26 August, with a coherent vorticity column extending from the surface to 400 hPa in the eastern portion (NWI), and values exceeding $14 \times 10^{-5} \text{ s}^{-1}$ in the core. A dramatic reorganization of the zonal wind structure occurred as this development created a pronounced cyclonic circulation, disrupting the previously more uniform zonal flow. The θ_e contours showed wrapping patterns consistent with warm-core development, representing classic warm-core development as described in Emanuel (1986) wind-induced surface heat exchange (WISHE) theory.

The system continued to strengthen through 1800 UTC 26 August, with the vorticity column now reaching 300 hPa and the zonal wind pattern showing the influence of the intensifying system with the upper-level jet appearing to retreat northward. The warm-core structure was clearly visible in the θ_e contours with pronounced wrapping patterns, causing significant modification of the zonal wind structure throughout the troposphere, developing a structure matching the conceptual model of a maturing monsoon depression described by Hunt et al. (2016, 2021). By 0000 UTC 27 August, the system reached a near-mature stage with an intense vorticity column extending from surface to 300 hPa with values exceeding $14 \times 10^{-5} \text{ s}^{-1}$ throughout. The zonal wind field was now strongly modified by the mature system, establishing a dominant cyclonic circulation, while the upper-level jet shifted slightly northward, maintaining strong zonal winds aloft but with significant perturbations in mid and lower levels. This represented the transformation from baroclinic to a more barotropic structure consistent with tropical cyclone intensification processes described by Montgomery and Smith (2017).

Peak intensity occurred at 0600 UTC 27 August, with extreme vorticity values (>16 × 10^{-5} s⁻¹) throughout the lower and middle troposphere. The zonal wind structure was completely reorganized around this intense vorticity maximum, with strong cyclonic circulation dominating the eastern portion of the domain, while the θ_e contours showed maximum thermal anomalies in the core, aligning with findings of Kotal et al. (2009) on characteristic vorticity magnitudes in intense monsoon depressions. At 1200 UTC on 27 August, the system exhibited a slight decrease in maximum vorticity intensity while retaining a coherent vertical structure. The cyclonic circulation maintained its dominance in the eastern portion, while the zonal flow showed signs of adjustment with the outward expansion of the circulation as indicated by the θ_e pattern, consistent with the maturation phase described by Yoon and Chen (2005), where radial expansion occurs following peak intensity.

Figure 13 displayed the time-pressure plot that reveals critical upper-tropospheric and jet dynamics driving the NWI rainfall event during 21–30 August, 2024. During 21–25 August, the upper atmosphere was dominated by negative vorticity in the 50–150 hPa region, indicating a jet streak's right entrance region. This upper-level anticyclonic circulation established conditions favorable for mass divergence aloft, consistent with the classical four-quadrant jet streak model described by Uccellini and Johnson (1979). 25–27 August showed an atmospheric response to this upper-level forcing as a strong upward motion developed on 25 August and intensified through 27 August. The upper-level divergence induced compensating lower-level convergence, triggering a deep vertical circulation cell. As Hoskins et al. (1985) demonstrated, this ageostrophic circulation maintains thermal wind balance in jet acceleration regions with strong BEC over the north of Tibetan Plateau. Positive vorticity emerged in the mid-to-lower troposphere (300–850 hPa) as convergence intensified near the surface, a process Koch and Dorian (1988) identified as critical for organizing mesoscale convective systems beneath upper-level jets.

During the mature phase (27–29 August), the system reached peak intensity with maximum upward motion exceeding 0.45 Pa/s on 27 August at 300–350 hPa. The upper-level jet dynamics maintained strong divergence aloft, sustaining intense vertical velocity coupling throughout the troposphere. This deep vertical circulation efficiently transported moisture upward, generating enhanced precipitation across NWI. As Doyle and Warner (1993) noted, such jet-induced ascent can amplify precipitation rates by 2–3 times compared to purely convective processes. The strong positive vorticity ($>2 \times 10^{-5} \text{ s}^{-1}$) reflected intensified low-level convergence resulting from jet-induced secondary circulation, a relationship quantified by Keyser and Shapiro (1986). The enhanced dynamic connection between upper-level and lower-level atmospheric flow patterns is with momentum-induced vertical velocity. Specifically, when the upper-level jet streak shifted position further north on 29–30 August, it weakened the upper-level divergence and led to reduced vertical coupling, thereby reducing the upward motion intensity and consequently diminishing the precipitation efficiency over NWI (Figures 8e, 11e

MAHENDRA ET AL. 22 of 29

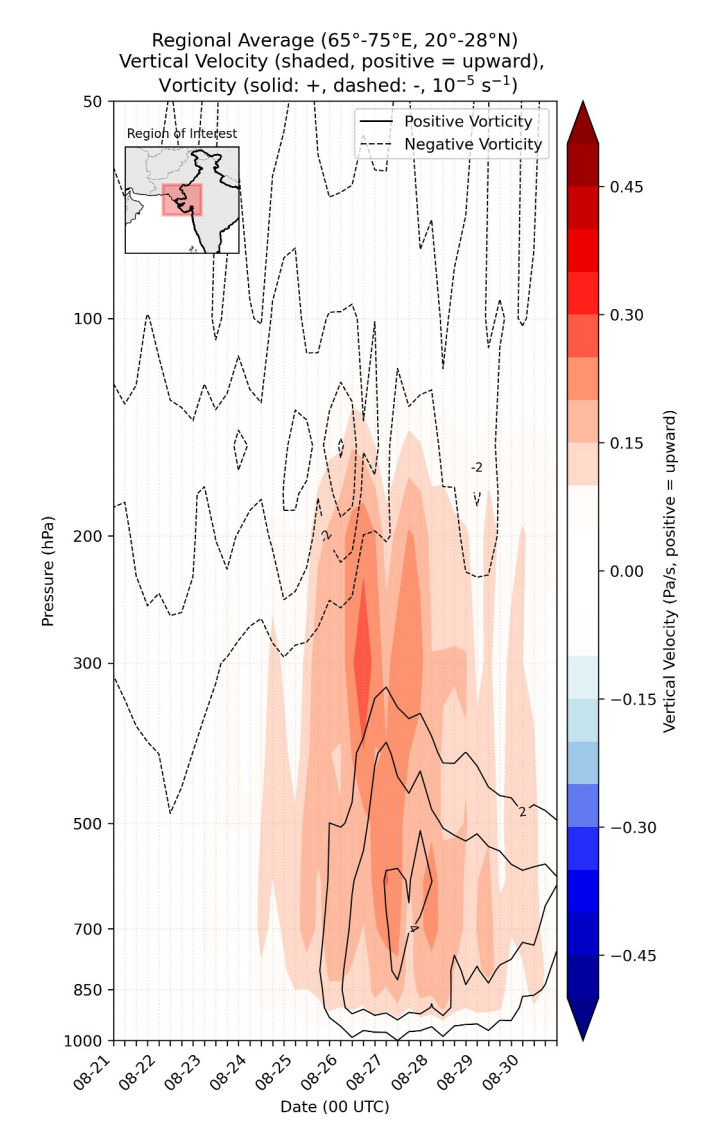


Figure 13. Time-pressure cross-section displaying vertical velocity and vorticity for the region $65^{\circ}-75^{\circ}\mathrm{E}$, $20^{\circ}-28^{\circ}\mathrm{N}$ during the August 2024 extreme rainfall event. The color shading represents vertical velocity (ω) ranging from -0.45 to $0.45\mathrm{Pa}~\mathrm{s}^{-1}$, with red indicating upward motion and blue showing downward motion. Solid black lines depict positive vorticity, while dashed lines represent negative vorticity, measured in $10^{-5}~\mathrm{s}^{-1}$. The analysis spans pressure levels from 1,000 to 50 hPa, capturing atmospheric dynamics from 21 August to 30 August 2024. The inset map highlights the specific geographical region of interest, providing spatial context for the vertical atmospheric profile.

and 13). Both upward motion and positive vorticity gradually diminished as the jet-induced forcing mechanism relaxed, following the typical lifecycle documented by Moore et al. (2019). This analysis captures how upper-level dynamics established the powerful vertical circulation mechanism that transported moisture upward and generated extreme precipitation over NWI, demonstrating the critical importance of upper-level forcing mechanisms as emphasized by Vellore et al. (2016) in their studies of extreme rainfall events over the Indian subcontinent.

4. Summary and Conclusions

Our comprehensive analysis of the August 2024 extreme rainfall event over NWI reveals a noteworthy interplay between midlatitude dynamics and tropical processes that overcame monsoon break conditions to produce exceptional precipitation. The schematic diagram (Figure 14) synthesizes our key findings, illustrating how the subtropical westerly jet streak created a favorable dynamic environment for extreme rainfall through enhanced thermally driven circulation in its entrance region, which directly contributed to the anomalous vertical motion observed. This jet streak configuration represents a larger-scale atmospheric pattern that appears to be increasingly influencing the spatial redistribution of monsoon rainfall over India, particularly enhancing precipitation over the northwestern regions. Additionally, this study has demonstrated how the spatial distribution of Indian monsoon rainfall is changing, with NWI receiving an increasing proportion of total monsoon rainfall (rising to 19.55% in 2024 compared to a historical average of 13.62% during 1981-2000). The August 2024 event exemplifies this shift, producing extreme rainfall during what would typically be monsoon break conditions over the broader Indian region. The event was characterized by anomalous rainfall over NWI during 21-30 August, 2024, with precipitation rates exceeding 100 mm day⁻¹ at peak intensity. While the broader Indian monsoon region experienced break conditions, NWI received concentrated heavy rainfall due to a unique configuration of atmospheric dynamics. Our probability density function analysis revealed that the 2024 summer monsoon season contribution of NWI to overall Indian rainfall (19.55%) fell at the extreme right tail of historical distributions, highlighting the exceptional nature of this event within the context of changing monsoon patterns.

Analysis also noted that complex moisture transport dynamics, manifesting as a strong three-channel system, fueled this extreme precipitation event. The first channel originated from the Bay of Bengal on 24 August, followed by continental moisture recycling through Central India on 25 August, and finally the third channel involved the western moisture conveyor from the Arabian Sea on 26 August. This multisource convergence created a critical zone of moisture accumulation around $20^{\circ}N-25^{\circ}N$. These converging moisture channels created ideal conditions for intense precipitation, prompting us to investigate the dominant physical mechanisms at work.

Detailed moisture budget analysis demonstrated that vertical moisture convergence dominated during this event, rather than the horizontal convergence that typically characterizes monsoon rainfall. The primary driver was the anomalous vertical motion acting upon the background moisture profile, highlighting the dominance of dynamical processes over purely thermodynamic factors in triggering this extreme event.

The global context for this event included significant SST anomalies, particularly in the North Atlantic $(1-3^{\circ}\text{C})$ above normal) and Arabian Sea $(0.5-2^{\circ}\text{C})$ above normal), and these thermal anomalies enhanced significant baroclinicity in midlatitudes at 500 hPa over North Atlantic. Surface air temperature analysis depicted a distinctive thermal dipole over the Indian region—cooling over NWI contrasted with warming over the Tibetan

MAHENDRA ET AL. 23 of 29

com/doi/10.1029/2025JD044227 by Kieran Hunt - NICE, National

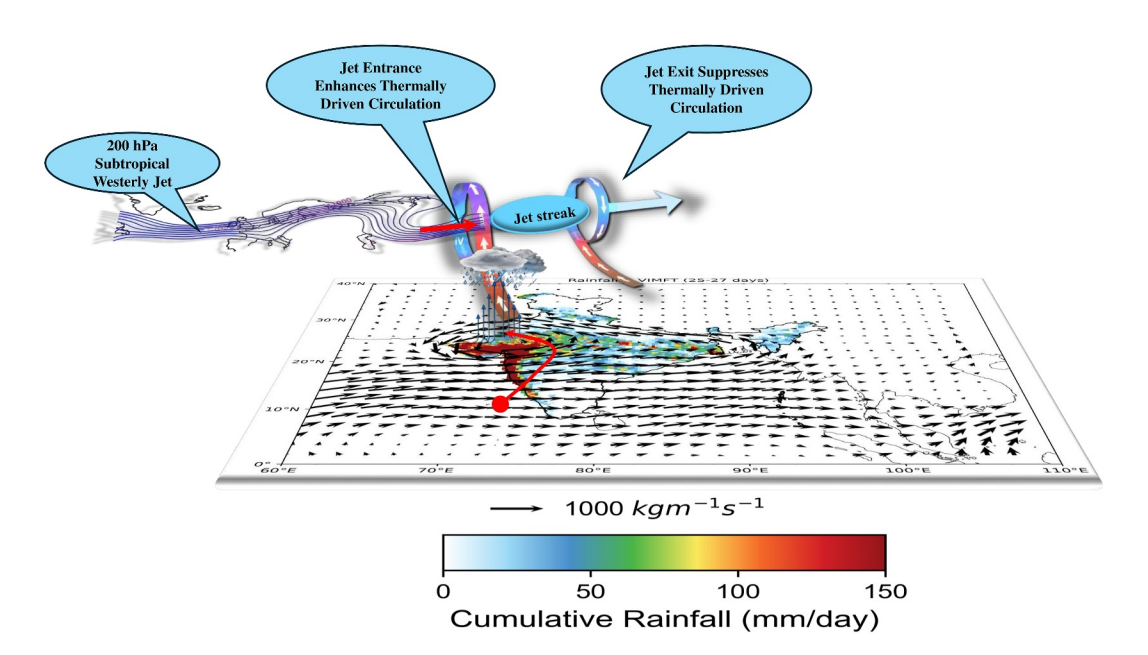


Figure 14. Schematic representation of the 200 hPa subtropical westerly jet stream's interaction with regional atmospheric circulation during the August 2024 extreme rainfall event. The image illustrates the complex interplay between jet stream dynamics and thermally driven circulation, highlighting key processes at different atmospheric levels. Color-coded rainfall intensity ranges from 0 to 150 mm day⁻¹, with vector fields showing atmospheric moisture transport (kg m⁻¹ s⁻¹).

Plateau—which increased atmospheric instability and enhanced vertical motion. The atmospheric circulation driving this event originated from enhanced baroclinic instability over the North Atlantic, with Eady growth rate values exceeding climatological means at both 500 hPa (0.67 day⁻¹) and 850 hPa (0.53 day⁻¹). This instability generated a Rossby wave train that propagated eastward along the midlatitude waveguide, as evidenced by LWA and WAF analysis. The development of a European/Ural blocking pattern between 21 and 26 August redirected energy downstream, establishing the large-scale flow configuration that ultimately affected NWI.

Our local wave activity and quasi-geostrophic potential vorticity analyses confirmed pronounced wave amplification (LWA exceeding 150 m s⁻¹) centered at 30°E on 25 August, with subsequent downstream development toward Central Asia. The downstream distorted Rossby waves broke recursively, triggering a pronounced Caspian Sea trough that deepened by 25-26 August, strengthening the subtropical jet streak north of the Tibetan Plateau. A critical aspect of this event was the development of the subtropical jet streak north of the Tibetan Plateau. Upper tropospheric analysis revealed intense wind speeds exceeding 120 m² s⁻² over Central Asia during 25-26 August. Through its right entrance region, this jet streak established an ageostrophic circulation cell that enhanced upward motion over NWI, creating a direct dynamical connection between midlatitude processes and tropical convection Figure 11. Time-pressure analysis showed that the upper-level divergence in the jet streak's right entrance region induced compensating lower-level convergence, triggering deep vertical motion that peaked at 0.45 Pa s⁻¹ on 26 to 27 August at 300–350 hPa. The jet streak's ageostrophic circulation not only enhanced vertical motion but also contributed to the development of the vorticity column, creating a feedback mechanism that further intensified the precipitation system. Vertical cross-section analysis detailed the progressive development of a coherent vorticity column extending from the surface to the upper troposphere. Beginning with scattered vorticity patches on 25 August, the system evolved to form an intense vorticity column by 27 August, with extreme values (> $16 \times 10^{-5} \text{ s}^{-1}$) throughout the troposphere. This vertical structure represented the complete coupling between upper-level dynamics and lower-level processes, enabling efficient moisture transport and precipitation generation. θ_e contours showed wrapping patterns consistent with warm core development, similar to the structure of intensifying monsoon depressions.

This event exemplifies the intensifying tropical-extratropical connectivity in our warming climate. As global temperatures continue to rise, we may expect increased frequency of similar events, particularly during summer periods. The spatial redistribution of monsoon rainfall, with increasing contributions from northwestern regions,

MAHENDRA ET AL. 24 of 29

Wiley Online Library on [07/11/2025].

aligns with IPCC model projections under high emission scenarios. Our findings highlight the critical need for improved understanding of tropical-extratropical interactions, as these connections increasingly drive extreme precipitation events with significant societal impacts. The interplay between midlatitude dynamics and tropical processes observed in this event, particularly the role of the subtropical westerly jet streak in overcoming monsoon break conditions, represents a physical mechanism that may become increasingly relevant in future climate scenarios in which changes in the North Atlantic may be evident. This analysis provides a foundation for future research, which will focus on detailed composites of similar events to establish more robust climatological patterns and explore the predictability of such events through the analysis of forecast model performance. The identification of specific jet streak configurations as precursors to such extreme events may provide valuable early warning indicators for operational forecasting. The schematic model presented here provides a conceptual framework for understanding the complex dynamical processes that generated this extreme rainfall event and offers insights into similar phenomena that may become more common as global climate changes.

Conflict of Interest

The authors declare no conflicts of interest relevant to this study.

Data Availability Statement

All data sets and diagnostics used in this research are publicly available. ERA5 reanalysis data can be accessed from https://cds.climate.copernicus.eu/datasets/reanalysis-era5-pressure-levels?tab=overview, IMD precipitation data from https://psl.noaa.gov/data/grid-ded/data.cpc.globalprecip.html, and SST data from NOAA OI SST V2 at https://psl.noaa.gov/data/gridded/data.noaa.oisst.v2.highres.html. The LWA Rossby Wave Diagnostics Python package is available at https://github.com/csyhuang/hn2016_falwa, and the moisture budget analysis code can be obtained from https://github.com/mahendrawrf/Moisture_Budget. Code availability: Python codes to generate figures in the analysis will be made available upon request to the first author.

Acknowledgments References

M. N and N. C acknowledge the founding support of the OVDF Fellowship (OVDF) Award No:SB/S9/Z-03/2017-XII (2023) by the ANRF, Government of India, MoEs research Grant MOES/9/2024-O/o PH (GI), and Purdue University. L.W. acknowledge funding support from a NOAA Modeling, Analysis, Predictions, and Projections (MAPP) award NA24OARX431C0054-T1-01. M.H. acknowledges funding from NSF OCE award 2217530. M. N. extends his sincere gratitude to NIT Rourkela and Purdue University for hosting him during his research stay and providing an excellent academic environment. He also thanks the reviewers for their constructive comments, which significantly enhanced the quality and robustness of this manuscript.

Acosta, R. P., & Huber, M. (2017). The neglected Indo-Gangetic plains low-level jet and its importance for moisture transport and precipitation during the peak summer monsoon. *Geophysical Research Letters*, 44(16), 8601–8610. https://doi.org/10.1002/2017GL074440

Ashok, K., Guan, Z., & Yamagata, T. (2001). Impact of the Indian Ocean dipole on the relationship between the Indian monsoon rainfall and ENSO. *Geophysical Research Letters*, 28(23), 4499–4502. https://doi.org/10.1029/2001GL013294

Athira, K. S., Roxy, M. K., Dasgupta, P., Saranya, J. S., Singh, V. K., & Attada, R. (2023). Regional and temporal variability of Indian summer monsoon rainfall in relation to El Niño southern oscillation. Scientific Reports, 13(1), 12643. https://doi.org/10.1038/s41598-023-38730-5

Bach, E., Krishnamurthy, V., Mote, S., Shukla, J., Sharma, A. S., Kalnay, E., & Ghil, M. (2024). Improved subseasonal prediction of South Asian monsoon rainfall using data-driven forecasts of oscillatory modes. *Proceedings of the National Academy of Sciences*, 121(15), e2312573121. https://doi.org/10.1073/pnas.2312573121

Barnes, E. A., & Screen, J. A. (2015). The impact of Arctic warming on the midlatitude jet-stream: Can it? Has it? Will it? Wiley Interdisciplinary Reviews: Climate Change, 6(3), 277–286. https://doi.org/10.1002/wcc.337

Bhatla, R., Mohanty, U. C., Raju, P. V. S., & Madan, O. P. (2004). A study on dynamic and thermodynamic aspects of breaks in the summer monsoon over India. *International Journal of Climatology*, 24(3), 341–360. https://doi.org/10.1002/joc.1005

Biswas, B. N., Chatterjee, S., Mukherjee, S. P., & Pal, S. (2013). A discussion on Euler method: A review. Tech. Rep. No. 2 (Vol. 1).

Bollasina, M. A., Ming, Y., & Ramaswamy, V. (2011). Anthropogenic aerosols and the weakening of the South Asian summer monsoon. *Science*, 334(6055), 502–505. https://doi.org/10.1126/science.1204994

Bordoni, S., & Schneider, T. (2008). Monsoons as eddy-mediated regime transitions of the tropical overturning circulation. *Nature Geoscience*, 1(8), 515–519. https://doi.org/10.1038/ngeo248

Branstator, G. (2002). Circumglobal teleconnections, the jet stream waveguide, and the North Atlantic oscillation. *Journal of Climate*, 15(14), 1893–1910. https://doi.org/10.1175/1520-0442(2002)015(1893:CTTJSW)2.0.CO;2

CarbonBrief. (2021). In-depth Q&A: The IPCC's sixth assessment report on climate science Carbon brief.

Chang, E. K. (2000). Wave packets and life cycles of troughs in the upper troposphere: Examples from the Southern Hemisphere summer season of 1984/85. Monthly Weather Review, 128(1), 25–50. https://doi.org/10.1175/1520-0493(2000)128(0025:WPALCO)2.0.CO;2

Chang, E. K. (2005). The impact of wave packets propagating across Asia on Pacific cyclone development. *Monthly Weather Review*, 133(7), 1998–2015. https://doi.org/10.1175/MWR2953.1

Chang, E. K., Lee, S., & Swanson, K. L. (2002). Storm track dynamics. *Journal of Climate*, 15(16). https://doi.org/10.1175/1520-0442(2002)015 (02163:STD)2.0.CO;2

Chang, E. K., & Yu, D. B. (1999). Characteristics of wave packets in the upper troposphere. Part I: Northern Hemisphere winter. *Journal of the Atmospheric Sciences*, 56(11), https://doi.org/10.1175/1520-0469(1999)056(1708:COWPIT)2.0.CO:2

Charney, J. G. (1947). The dynamics of long waves in a baroclinic westerly current. *Journal of Meteorology*, 4(5), 136–162. https://doi.org/10.1175/1520-0469(1947)004(0136:tdolwi)2.0.co;2

Chen, M., Shi, W., Xie, P., Silva, V. B., Kousky, V. E., Higgins, R. W., & Janowiak, J. E. (2008). Assessing objective techniques for gauge-based analyses of global daily precipitation. *Journal of Geophysical Research*, 113(4). https://doi.org/10.1029/2007JD009132

MAHENDRA ET AL. 25 of 29

- Chen, T. C., Yen, M. C., & Weng, S. P. (2000). Interaction between the summer monsoons in East Asia and the South China Sea: Intraseasonal monsoon modes. *Journal of the Atmospheric Sciences*, 57(9). https://doi.org/10.1175/1520-0469(2000)057(1373:IBTSMI)2.0.CO;2
- Chen, X., Luo, D., Feldstein, S. B., & Lee, S. (2018). Impact of winter Ural blocking on Arctic sea ice: Short-time variability. *Journal of Climate*, 31(6), 2267–2282. https://doi.org/10.1175/JCLI-D-17-0194.1
- Chen, X., Luo, D., Wu, Y., Dunn-Sigouin, E., & Lu, J. (2021). Nonlinear response of atmospheric blocking to early winter Barents-Kara seas warming: An idealized model study. *Journal of Climate*, 34(6), 2367–2383. https://doi.org/10.1175/JCLI-D-19-0720.1
- Chilukoti, N., Nimmakanti, M., & Chowdary, J. S. (2024). Recent two decades witness an uptick in monsoon depressions over the northern Arabian Sea. npj Climate and Atmospheric Science, 7(1), 183. https://doi.org/10.1038/s41612-024-00727-w
- Chowdary, J. S., Xie, S. P., & Nanjundiaha, R. S. (2021). Drivers of the Indian summer monsoon climate variability. In *Indian summer monsoon variability: El Niño-teleconnections and beyond*. https://doi.org/10.1016/B978-0-12-822402-1.00020-X
- Cohen, J., Zhang, X., Francis, J., Jung, T., Kwok, R., Overland, J., et al. (2018). Arctic change and possible influence on mid-latitude climate and weather: A us Clivar white paper. US CLIVAR reports. https://doi.org/10.5065/D6TH8KGW
- Coumou, D., Di Capua, G., Vavrus, S., Wang, L., & Wang, S. (2018). The influence of Arctic amplification on mid-latitude summer circulation. *Nature Communications*, 9(1), 2959. https://doi.org/10.1038/s41467-018-05256-8
- Dimri, A. P., Niyogi, D., Barros, A. P., Ridley, J., Mohanty, U. C., Yasunari, T., & Sikka, D. R. (2015). Western disturbances: A review. Reviews of Geophysics, 53(2), 225–246. https://doi.org/10.1002/2014RG000460
- Ding, Q., & Wang, B. (2005). Circumglobal teleconnection in the Northern Hemisphere summer. *Journal of Climate*, 18(17), 3483–3505. https://doi.org/10.1175/JCL13473.1
- Ding, Q., & Wang, B. (2007). Intraseasonal teleconnection between the summer Eurasian wave train and the Indian monsoon. *Journal of Climate*, 20(15), 3751–3767. https://doi.org/10.1175/JCLI4221.1
- Dong, W., Lin, Y., Wright, J. S., Xie, Y., Xu, F., Yang, K., et al. (2018). Connections between a late summer snowstorm over the Southwestern Tibetan Plateau and a concurrent Indian monsoon low-pressure system. *Journal of Geophysical Research: Atmospheres*, 123(24). https://doi.org/10.1029/2018ID029710
- Doyle, J. D., & Warner, T. T. (1993). A three-dimensional numerical investigation of a Carolina coastal low-level jet during GALE IOP 2. *Monthly Weather Review*, 121(4). https://doi.org/10.1175/1520-0493(1993)121(1030:ATDNIO)2.0.CO;2
- Duchon, C. E. (1979). Lanczos filtering in one and two dimensions. *Journal of Applied Meteorology*, 18(8), 1016–1022. https://doi.org/10.1175/1520-0450(1979)018(1016:LFIOAT)2.0.CO;2
- Dunkerton, T. J., Montgomery, M. T., & Wang, Z. (2009). Tropical cyclogenesis in a tropical wave critical layer: Easterly waves. *Atmospheric Chemistry and Physics*, 9(15), 5587–5646. https://doi.org/10.5194/acp-9-5587-2009
- Eady, E. T. (1949). Long waves and cyclone waves. Tellus, 1(3), 33-52. https://doi.org/10.3402/tellusa.v1i3.8507
- Emanuel, K. A. (1986). An air-sea interaction theory for tropical cyclones. Part I: Steady-state maintenance. *Journal of the Atmospheric Sciences*, 43(6), 585–605. https://doi.org/10.1175/1520-0469(1986)043\0585:aasitf\2.0.co;2
- Feba, F., Ashok, K., & Ravichandran, M. (2019). Role of changed Indo-Pacific atmospheric circulation in the recent disconnect between the Indian summer monsoon and ENSO. Climate Dynamics, 52(3–4), 1461–1470. https://doi.org/10.1007/s00382-018-4207-2
- Francis, J. A., & Vavrus, S. J. (2012). Evidence linking Arctic amplification to extreme weather in mid-latitudes. *Geophysical Research Letters*, 39(6), https://doi.org/10.1029/2012GL051000
- Gadgil, S., & Gadgil, S. (2006). The Indian monsoon, GDP and agriculture. *Economic and Political Weekly*. https://www.jstor.org/stable/4418949 Gadgil, S., & Joseph, P. V. (2003). On breaks of the Indian monsoon. *Journal of Earth System Science*, 112(4), 529–558. https://doi.org/10.1007/BE02700778
- Glatt, I., Dörnbrack, A., Jones, S., Keller, J., Martius, O., Müller, A., et al. (2011). Utility of Hovmöller diagrams to diagnose Rossby wave trains. Tellus, Series A: Dynamic Meteorology and Oceanography, 63(5), 991. https://doi.org/10.1111/j.1600-0870.2011.00541.x
- Glatt, I., & Wirth, V. (2014). Identifying Rossby wave trains and quantifying their properties. Quarterly Journal of the Royal Meteorological Society, 140(679), 384–396. https://doi.org/10.1002/qi.2139
- Goswami, B. N., Chakraborty, D., Rajesh, P. V., & Mitra, A. (2022). Predictability of South-Asian monsoon rainfall beyond the legacy of Tropical Ocean Global Atmosphere program (TOGA). npj Climate and Atmospheric Science, 5(1), 58. https://doi.org/10.1038/s41612-022-00281-3
- Goswami, B. N., Venugopal, V., Sangupta, D., Madhusoodanan, M. S., & Xavier, P. K. (2006). Increasing trend of extreme rain events over India in a warming environment. *Science*, 314(5804), 1442–1445. https://doi.org/10.1126/science.1132027
- Goswami, B. N., & Xavier, P. K. (2005). ENSO control on the south Asian monsoon through the length of the rainy season. Geophysical Research Letters, 32(18). https://doi.org/10.1029/2005GL023216
- Hagos, S., Zhang, C., Tao, W. K., Lang, S., Takayabu, Y. N., Shige, S., et al. (2010). Estimates of tropical diabatic heating profiles: Commonalities and uncertainties. *Journal of Climate*, 23(3), 542–558. https://doi.org/10.1175/2009JCLI3025.1
- Hartmann, D. L. (2015). Global physical climatology (2nd ed.). https://doi.org/10.1016/C2009-0-00030-0
- Hersbach, H., Bell, B., Berrisford, P., Biavati, G., Horányi, A., Sabater, J. M., et al. (2023). ERA5 hourly data on single levels from 1940 to present [Dataset]. Copernicus Climate Change Service (C3S) Climate Data Store (CDS), 147(741). https://cds.climate.copernicus.eu/datasets/reanalysis-era5-single-levels?tab=overview
- Hoskins, B. J., & Ambrizzi, T. (1993). Rossby wave propagation on a realistic longitudinally varying flow. *Journal of the Atmospheric Sciences*, 50(12). https://doi.org/10.1175/1520-0469(1993)050(1661:RWPOAR)2.0.CO;2
- Hoskins, B. J., & Hodges, K. I. (2019). The annual cycle of Northern Hemisphere storm tracks. Part I: Seasons. *Journal of Climate*, 32(6), 1743–1760. https://doi.org/10.1175/JCLI-D-17-0870.1
- Hoskins, B. J., McIntyre, M. E., & Robertson, A. W. (1985). On the use and significance of isentropic potential vorticity maps. *The Quarterly Journal of the Royal Meteorological Society*, 111(466). https://doi.org/10.1002/qj.49711146602
- Hoskins, B. J., & Valdes, P. J. (1990). On the existence of storm-tracks. *Journal of the Atmospheric Sciences*, 47(15). https://doi.org/10.1175/1520-0469(1990)047(1854:OTEOST)2.0.CO;2
- Houze, R. A., McMurdie, L. A., Rasmussen, K. L., Kumar, A., & Chaplin, M. M. (2017). Multiscale aspects of the storm producing the June 2013 flooding in Uttarakhand, India. *Monthly Weather Review*, 145(11), 4447–4466. https://doi.org/10.1175/MWR-D-17-0004.1
- Huang, B., Liu, C., Banzon, V., Freeman, E., Graham, G., Hankins, B., et al. (2021). Improvements of the Daily Optimum Interpolation Sea Surface Temperature (DOISST) version 2.1. *Journal of Climate*, 34(8), 2923–2939. https://doi.org/10.1175/JCLI-D-20-0166.1
- Huang, C. S. Y., & Nakamura, N. (2016). Local finite-amplitude wave activity as a diagnostic of anomalous weather events. *Journal of the Atmospheric Sciences*, 73(1), 211–229. https://doi.org/10.1175/JAS-D-15-0194.1
- Hunt, K. M. R. (2024). Increasing frequency and lengthening season of western disturbances are linked to increasing strength and delayed northward migration of the subtropical jet. Weather and Climate Dynamics, 5(1), 345–356. https://doi.org/10.5194/wcd-5-345-2024

MAHENDRA ET AL. 26 of 29

- Hunt, K. M. R., & Turner, A. G. (2017). The effect of horizontal resolution on Indian monsoon depressions in the met Office NWP model. Quarterly Journal of the Royal Meteorological Society, 143(705), 1756–1771. https://doi.org/10.1002/qj.3030
- Hunt, K. M. R., Turner, A. G., Inness, P. M., Parker, D. E., & Levine, R. C. (2016). On the structure and dynamics of Indian monsoon depressions. Monthly Weather Review, 144(9), 3391–3416. https://doi.org/10.1175/MWR-D-15-0138.1
- Hunt, K. M. R., Turner, A. G., & Schiemann, R. K. (2021). How interactions between tropical depressions and western disturbances affect heavy precipitation in south Asia. Monthly Weather Review, 149(6). https://doi.org/10.1175/MWR-D-20-0373.1
- Hunt, K. M. R., Turner, A. G., & Shaffrey, L. C. (2018a). The evolution, seasonality and impacts of western disturbances. Quarterly Journal of the Royal Meteorological Society, 144(710), 278–290. https://doi.org/10.1002/qj.3200
- Hunt, K. M. R., Turner, A. G., & Shaffrey, L. C. (2018b). Extreme daily rainfall in Pakistan and North India: Scale interactions, mechanisms, and precursors. Monthly Weather Review, 146(4), 1005–1022. https://doi.org/10.1175/MWR-D-17-0258.1
- Joseph, L., Skliris, N., Dey, D., Marsh, R., & Hirschi, J. (2024). Increased summer monsoon rainfall over Northwest India caused by Hadley cell expansion and Indian Ocean warming. *Geophysical Research Letters*, 51(16), e2024GL108829. https://doi.org/10.1029/2024GL108829
- Karmakar, N., Joseph, S., & Sahai, A. K. (2022). Northward propagation of convection over Arabian Sea and Bay of Bengal: A perspective from vorticity equation. Climate Dynamics, 59(9–10), 2751–2767. https://doi.org/10.1007/s00382-022-06248-7
- Keyser, D., & Shapiro, M. A. (1986). A review of the structure and dynamics of upper-level frontal zones. *Monthly Weather Review*, 114(2). https://doi.org/10.1175/1520-0493(1986)114(0452:AROTSA)2.0.CO;2
- Koch, S. E., & Dorian, P. B. (1988). A mesoscale gravity wave event observed during CCOPE. Part III: Wave environment and probable source mechanisms. Monthly Weather Review, 116(12). https://doi.org/10.1175/1520-0493(1988)116(2570:AMGWEO)2.0.CO;2
- Kornhuber, K., Petoukhov, V., Petri, S., Rahmstorf, S., & Coumou, D. (2017). Evidence for wave resonance as a key mechanism for generating high-amplitude quasi-stationary waves in boreal summer. Climate Dynamics, 49(5–6), 1961–1979. https://doi.org/10.1007/s00382-016-3399-6
- Kosaka, Y., & Nakamura, H. (2010). Mechanisms of meridional teleconnection observed between a summer monsoon system and a subtropical anticyclone. Part II: A global survey. *Journal of Climate*, 23(19), 5109–5125. https://doi.org/10.1175/2010JCLI3414.1
- Kotal, S. D., Kundu, P. K., & Roy Bhowmik, S. K. (2009). Analysis of cyclogenesis parameter for developing and nondeveloping low-pressure systems over the Indian Sea. Natural Hazards, 50(2), 389–402. https://doi.org/10.1007/s11069-009-9348-5
- Kripalani, R. H., & Kulkarni, A. (1997). Climatic impact of El Niño/La Niña on the Indian monsoon: A new perspective. Weather, 52(2), 39–46. https://doi.org/10.1002/j.1477-8696.1997.tb06267.x
- Krishnamurthy, V. (2019). Predictability of weather and climate. Earth and Space Science, 6(7), 1043–1056. https://doi.org/10.1029/2019EA000586
- Krishnamurthy, V., & Goswami, B. N. (2000). Indian monsoon-ENSO relationship on interdecadal timescale. *Journal of Climate*, 13(3). https://doi.org/10.1175/1520-0442(2000)013(0579:IMEROI)2.0.CO;2
- doi.org/10.1175/1520-0442(2000)013(0579:IMEROI)2.0.CO;2
 Krishnamurti, T. N., Thomas, A., Simon, A., & Kumar, V. (2010). Desert air incursions, an overlooked aspect, for the dry spells of the Indian
- summer monsoon. *Journal of the Atmospheric Sciences*, 67(10), 3423–3441. https://doi.org/10.1175/2010JAS3440.1

 Krishnan, R., Kumar, V., Sugi, M., & Yoshimura, J. (2009). Internal feedbacks from monsoon-midlatitude interactions during droughts in the
- Indian summer monsoon. Journal of the Atmospheric Sciences, 66(3), 553–578. https://doi.org/10.1175/2008JAS2723.1
- Krishnan, R., Sanjay, J., Gnanaseelan, C., Mujumdar, M., Kulkarni, A., & Chakraborty, S. (2020). Assessment of climate change over the Indian region: A report of the Ministry Of Earth Sciences (MOES). Government of India. https://doi.org/10.1007/978-981-15-4327-2
- Krishnan, R., & Sugi, M. (2001). Baiu rainfall variability and associated monsoon teleconnections. Journal of the Meteorological Society of Japan. Ser. II, 79(3), 851–860. https://doi.org/10.2151/jmsj.79.851
- Kulkarni, A., Sabin, T. P., Chowdary, J. S., KoteswaraRao, K., Priya, P., Gandhi, N., et al. (2020). Precipitation changes in India. In Assessment of climate change over the Indian region: A report of the Ministry Of Earth Sciences (MOES). Government of India. https://doi.org/10.1007/978-981-15-4327-2.
- Kumar, K. K., Rajagopalan, B., & Cane, M. A. (1999). On the weakening relationship between the Indian monsoon and ENSO. *Science*, 284(5423), 2156–2159. https://doi.org/10.1126/science.284.5423.2156
- Lau, W. K., & Kim, K. M. (2012). The 2010 Pakistan flood and Russian heat wave: Teleconnection of hydrometeorological extremes. *Journal of Hydrometeorology*, 13(1), 392–403. https://doi.org/10.1175/JHM-D-11-016.1
- Li, B., Zhou, L., Qin, J., Zhou, T., Chen, D., Hou, S., & Murtugudde, R. (2023). Middle East warming in spring enhances summer rainfall over Pakistan. *Nature Communications*, 14(1), 7635. https://doi.org/10.1038/s41467-023-43463-0
- Li, K.-Y., & Liu, W. (2025). Weakened Atlantic Meridional overturning circulation causes the historical north Atlantic warming hole. Communications Earth and Environment, 6(1), 416. https://doi.org/10.1038/s43247-025-02403-0
- Lindzen, R. S., & Farrell, B. (1980). A simple approximate result for the maximum growth rate of baroclinic instabilities. *Journal of the Atmospheric Sciences*, 37(7). https://doi.org/10.1175/1520-0469(1980)037\(\frac{1648:ASARFT}{2.0.CO;2}\)
- Lubis, S. W., Hagos, S., Chang, C. C., Balaguru, K., & Leung, L. R. (2023). Cross-equatorial surges boost MJO's southward detour over the maritime continent. *Geophysical Research Letters*, 50(15), e2023GL104770. https://doi.org/10.1029/2023GL104770
- Luo, D., Chen, X., & Feldstein, S. B. (2018). Linear and nonlinear dynamics of North Atlantic oscillations: A new thinking of symmetry breaking. Journal of the Atmospheric Sciences, 75(6), 1955–1977. https://doi.org/10.1175/JAS-D-17-0274.1
- Madhura, R. K., Krishnan, R., Revadekar, J. V., Mujumdar, M., & Goswami, B. N. (2015). Changes in western disturbances over the Western Himalayas in a warming environment. Climate Dynamics, 44(3–4), 1157–1168. https://doi.org/10.1007/s00382-014-2166-9
- Mahendra, N., Chilukoti, N., & Chowdary, J. S. (2024). The increased summer monsoon rainfall in northwest India: Coupling with the northwestern Arabian sea warming and modulated by the silk road pattern since 2000. Atmospheric Research, 297, 107094. https://doi.org/10.1016/j.atmosres.2023.107094
- Mahendra, N., Nagaraju, C., Chowdary, J. S., Ashok, K., & Singh, M. (2023). A curious case of the Indian summer monsoon 2020: The influence of barotropic Rossby waves and the monsoon depressions. Atmospheric Research, 281, 106476. https://doi.org/10.1016/j.atmosres.2022. 106476.
- Mahendra, N., Sriranga, C. J., Patekar, D., Pilli, S., Anant, P., & Chellappan, G. (2021). Interdecadal modulation of interannual ENSO-Indian summer monsoon rainfall teleconnections in observations and CMIP6 models: Regional patterns. *International Journal of Climatology*, 41(4), 2528–2552. https://doi.org/10.1002/joc.6973
- Mak, M., & Cai, M. (1989). Local barotropic instability. *Journal of the Atmospheric Sciences*, 46(21). https://doi.org/10.1175/1520-0469(1989) 046(3289:LBI)2.0.CO;2
- Mann, M. E., Rahmstorf, S., Kornhuber, K., Steinman, B. A., Miller, S. K., & Coumou, D. (2017). Influence of anthropogenic climate change on planetary wave resonance and extreme weather events. *Scientific Reports*, 7(1), 45242. https://doi.org/10.1038/srep45242
- Martius, O., Schwierz, C., & Davies, H. C. (2008). Far-upstream precursors of heavy precipitation events on the Alpine south-side. Quarterly Journal of the Royal Meteorological Society, 134(631 PART B), 417–428. https://doi.org/10.1002/qj.229

MAHENDRA ET AL. 27 of 29

- Martius, O., Sodemann, H., Joos, H., Pfahl, S., Winschall, A., Croci-Maspoli, M., et al. (2013). The role of upper-level dynamics and surface processes for the Pakistan flood of July 2010. Quarterly Journal of the Royal Meteorological Society, 139(676), 1780–1797. https://doi.org/10. 1002/ai.2082
- Mishra, V., Nanditha, J. S., Dangar, S., Chuphal, D. S., & Vegad, U. (2024). Drivers, changes, and impacts of hydrological extremes in India: A review. WIREs Water, 11(5), e1742. https://doi.org/10.1002/wat2.1742
- Montgomery, M. T., & Smith, R. K. (2017). Recent developments in the fluid dynamics of tropical cyclones. *Annual Review of Fluid Mechanics*, 49(1), 541–574. https://doi.org/10.1146/annurev-fluid-010816-060022
- Moore, B. J., Keyser, D., & Bosart, L. F. (2019). Linkages between extreme precipitation events in the central and eastern United States and Rossby wave breaking. *Monthly Weather Review*, 147(9), 3327–3349. https://doi.org/10.1175/MWR-D-19-0047.1
- Moron, V., Robertson, A. W., & Boer, R. (2009). Spatial coherence and seasonal predictability of monsoon onset over Indonesia. *Journal of Climate*, 22(3), 840–850. https://doi.org/10.1175/2008JCL12435.1
- Murthy, V. S., & Boos, W. R. (2018). Role of surface enthalpy fluxes in idealized simulations of tropical depression Spinup. *Journal of the Atmospheric Sciences*, 75(6), 1811–1831. https://doi.org/10.1175/JAS-D-17-0119.1
- Nakamura, H., & Fukamachi, T. (2004). Evolution and dynamics of summertime blocking over the Far East and the associated surface Okhotsk high. *Quarterly Journal of the Royal Meteorological Society*, 130(599 PART B), 1213–1233. https://doi.org/10.1256/qj.03.101
- Nakamura, H., & Wallace, J. M. (1993). Synoptic behavior of baroclinic eddies during the blocking onset. *Monthly Weather Review*, 121(7). https://doi.org/10.1175/1520-0493(1993)121(1892:SBOBED)2.0.CO;2
- Nakamura, N., & Huang, C. S. (2018). Atmospheric blocking as a traffic jam in the jet stream. Science, 361(6397), 42–47. https://doi.org/10.1126/science.aat0721
- Nakamura, N., & Solomon, A. (2010). Finite-amplitude wave activity and mean flow adjustments in the atmospheric general circulation. Part I: Quasigeostrophic theory and analysis. *Journal of the Atmospheric Sciences*, 67(12), 3967–3983. https://doi.org/10.1175/2010JAS3503.1
- Nanditha, J. S., Kushwaha, A. P., Singh, R., Malik, I., Solanki, H., Chuphal, D. S., et al. (2023). The Pakistan Flood of August 2022: Causes and implications. Earth's Future, 11(3), e2022EF003230. https://doi.org/10.1029/2022EF003230
- O'Reilly, C. H., Minobe, S., Kuwano-Yoshida, A., & Woollings, T. (2017). The gulf stream influence on wintertime North Atlantic jet variability. Quarterly Journal of the Royal Meteorological Society, 143(702), 173–183. https://doi.org/10.1002/qj.2907
- Orlanski, I., & Chang, E. K. (1993). Ageostrophic geopotential fluxes in downstream and upstream development of baroclinic waves. *Journal of the Atmospheric Sciences*, 50(2). https://doi.org/10.1175/1520-0469(1993)050(0212:AGFIDA)2.0.CO;2
- Orlanski, I., & Sheldon, J. P. (1995). Stages in the energetics of baroclinic systems. *Tellus*, 47(5), 605. https://doi.org/10.3402/tellusa.v47i5.11553
 Pai, D. S., Sridhar, L., Badwaik, M. R., & Rajeevan, M. (2015). Analysis of the daily rainfall events over India using a new long period (1901–2010) high resolution (0.25° x 0.25°) gridded rainfall data set. *Climate Dynamics*, 45(3–4), 755–776. https://doi.org/10.1007/s00382-014-2307-1
- Pai, D. S., Sridhar, L., Rajeevan, M., Sreejith, O. P., Satbhai, N. S., & Mukhopadhyay, B. (2014). Development of a new high spatial resolution (0.25° x 0.25°) long period (1901–2010) daily gridded rainfall data set over India and its comparison with existing data sets over the region. *Mausam*, 65(1), 1–18. https://doi.org/10.54302/mausam.v65i1.851
- Parker, D. J., Willetts, P., Birch, C., Turner, A. G., Marsham, J. H., Taylor, C. M., et al. (2016). The interaction of moist convection and mid-level dry air in the advance of the onset of the Indian monsoon. *Quarterly Journal of the Royal Meteorological Society*, 142(699), 2256–2272. https://doi.org/10.1002/qj.2815
- Pathak, A., Ghosh, S., Alejandro Martinez, J., Dominguez, F., & Kumar, P. (2017). Role of oceanic and land moisture sources and transport in the seasonal and interannual variability of summer monsoon in India. *Journal of Climate*, 30(5), 1839–1859. https://doi.org/10.1175/JCLI-D-16-01561
- Pelly, J. L., & Hoskins, B. J. (2003). A new perspective on blocking. *Journal of the Atmospheric Sciences*, 60(5). https://doi.org/10.1175/1520-0469(2003)060(0743:ANPOB)2.0.CO;2
- Pottapinjara, V., Girishkuma, M. S., Ravichandran, M., & Murtugudde, R. (2014). Influence of the Atlantic zonal mode on monsoon depressions in the Bay of Bengal during boreal summer. *Journal of Geophysical Research*, 119(11), 6456–6469. https://doi.org/10.1002/2014JD021494
- Pradhan, M., Rao, A. S., Srivastava, A., Dakate, A., Salunke, K., & Shameera, K. S. (2017). Prediction of Indian summer-monsoon onset variability: A season in advance. *Scientific Reports*, 7(1), 14229. https://doi.org/10.1038/s41598-017-12594-y
- Priya, P., Krishnan, R., Mujumdar, M., & Houze, R. A. (2017). Changing monsoon and midlatitude circulation interactions over the Western Himalayas and possible links to occurrences of extreme precipitation. *Climate Dynamics*, 49(7–8), 2351–2364. https://doi.org/10.1007/s00382-016-3458-z
- Rahmstorf, S. (2024). Is the Atlantic overturning circulation approaching a tipping point? *Oceanography*, 37(3), 16–29. https://doi.org/10.5670/oceanog.2024.501
- Rahmstorf, S., Box, J. E., Feulner, G., Mann, M. E., Robinson, A., Rutherford, S., & Schaffernicht, E. J. (2015). Exceptional twentieth-century slowdown in Atlantic Ocean overturning circulation. *Nature Climate Change*, 5(5), 475–480. https://doi.org/10.1038/nclimate2554
- Rajeevan, M., Gadgil, S., & Bhate, J. (2010). Active and break spells of the Indian summer monsoon. *Journal of Earth System Science*, 119(3), 229–247. https://doi.org/10.1007/s12040-010-0019-4
- Rajeevan, M., Madhulatha, A., Rajasekhar, M., Bhate, J., Kesarkar, A., & Appa Rao, B. V. (2012). Development of a perfect prognosis probabilistic model for prediction of lightning over South-East India. *Journal of Earth System Science*, 121(2), 355–371. https://doi.org/10.1007/s12040-012-0173-y
- Ramaswamy, C. (1962). Breaks in the Indian summer monsoon as a phenomenon of interaction between the easterly and the sub-tropical westerly jet streams. *Tellus*, 14(3), 337–349. https://doi.org/10.1111/j.2153-3490.1962.tb01346.x
- Raymond, D. J., Sessions, S. L., & López Carrillo, C. (2011). Thermodynamics of tropical cyclogenesis in the northwest Pacific. *Journal of Geophysical Research*, 116(18), D18101. https://doi.org/10.1029/2011JD015624
- Rossby, C. G. (2020). Relation between variations in the intensity of the zonal circulation of the atmosphere and the displacements of the semi-permanent centers of action. *Journal of Marine Research*, 78(1), 38–55. https://doi.org/10.1357/002224039806649023
- Roxy, M. K., Ghosh, S., Pathak, A., Athulya, R., Mujumdar, M., Murtugudde, R., et al. (2017). A threefold rise in widespread extreme rain events over central India. *Nature Communications*, 8(1), 708. https://doi.org/10.1038/s41467-017-00744-9
- Saini, R., & Attada, R. (2024). Deciphering the characteristics and drivers of the summer monsoon precipitation extremes over the Indian Himalayas. *Journal of Geophysical Research: Atmospheres*, 129(20), e2024JD042226. https://doi.org/10.1029/2024jd042226
- Himalayas. *Journal of Geophysical Research: Atmospheres, 129*(20), e2024JD042226. https://doi.org/10.1029/2024jd042226 Scaife, A. A., Comer, R. E., Dunstone, N. J., Knight, J. R., Smith, D. M., MacLachlan, C., et al. (2017). Tropical rainfall, Rossby waves and
- regional winter climate predictions. *Quarterly Journal of the Royal Meteorological Society*, 143(702), 1–11. https://doi.org/10.1002/qj.2910
 Seager, R., Naik, N., & Vecchi, G. A. (2010). Thermodynamic and dynamic mechanisms for large-scale changes in the hydrological cycle in response to global warming. *Journal of Climate*, 23(17), 4651–4668. https://doi.org/10.1175/2010JCLI3655.1

MAHENDRA ET AL. 28 of 29

- Shaw, T. A., Baldwin, M., Barnes, E. A., Caballero, R., Garfinkel, C. I., Hwang, Y. T., et al. (2016). Storm track processes and the opposing influences of climate change, Nature Geoscience, 9(9), 656-664, https://doi.org/10.1038/ngeo2783
- Singh, R., Jaiswal, N., & Kishtawal, C. M. (2022). Rising surface pressure over Tibetan Plateau strengthens Indian summer monsoon rainfall over northwestern India. Scientific Reports, 12(1), 8621. https://doi.org/10.1038/s41598-022-12523-8
- Stohl, A. (1998). Computation, accuracy and applications of trajectories—A review and bibliography. Atmospheric Environment, 32(6), 947–966. https://doi.org/10.1016/S1352-2310(97)00457-3
- Takaya, K., & Nakamura, H. (2001). A formulation of a phase-independent wave-activity flux for stationary and migratory quasigeostrophic eddies on a zonally varying basic flow. Journal of the Atmospheric Sciences, 58(6). https://doi.org/10.1175/1520-0469(2001)058(0608: AFOAPI\2.0.CO;2
- Todd, R. E., & Ren, A. S. (2023). Warming and lateral shift of the Gulf stream from in situ observations since 2001. Nature Climate Change, 13(12), 1348-1352. https://doi.org/10.1038/s41558-023-01835-w
- Trenberth, K. E., Fasullo, J. T., & Mackaro, J. (2011). Atmospheric moisture transports from ocean to land and global energy flows in reanalyses. Journal of Climate, 24(18), 4907-4924. https://doi.org/10.1175/2011JCLI4171.1
- Turner, A. G., & Annamalai, H. (2012). Climate change and the South Asian summer monsoon. Nature Climate Change, 2(8), 587–595. https:// doi.org/10.1038/nclimate1495
- Uccellini, L. W., & Johnson, D. R. (1979). The coupling of upper and lower tropospheric jet streaks and implications for the development of severe convective storms. *Monthly Weather Review*, 107(6). https://doi.org/10.1175/1520-0493(1979)107(0682:tcoual)2.0.co;2
- Vellore, R. K., Kaplan, M. L., Krishnan, R., Lewis, J. M., Sabade, S., Deshpande, N., et al. (2016). Monsoon-extratropical circulation interactions in Himalayan extreme rainfall, Climate Dynamics, 46(11-12), 3517-3546, https://doi.org/10.1007/s00382-015-2784-x
- Vellore, R. K., Krishnan, R., Pendharkar, J., Choudhury, A. D., & Sabin, T. P. (2014). On the anomalous precipitation enhancement over the Himalayan foothills during monsoon breaks. Climate Dynamics, 43(7-8), 2009-2031. https://doi.org/10.1007/s00382-013-2024-1
- Vibhute, A. S., Chowdary, J. S., Darshana, P., Park, H. S., Rao, K. K., Parekh, A., & Gnanaseelan, C. (2023). Abrupt sub-seasonal rainfall variability over India during summer monsoon 2021: Interaction between midlatitude and tropical circulation. Atmospheric Research, 292, 106869, https://doi.org/10.1016/j.atmosres.2023.106869
- Vishnu, S., Francis, P. A., Shenoi, S. S., & Ramakrishna, S. S. (2016). On the decreasing trend of the number of monsoon depressions in the Bay of Bengal, Environmental Research Letters, 11(1), 014011, https://doi.org/10.1088/1748-9326/11/1/014011
- Wang, B., Biasutti, M., Byrne, M. P., Castro, C., Chang, C. P., Cook, K., et al. (2021). Monsoons climate change assessment. Bulletin of the American Meteorological Society, 102(1), E1-E19. https://doi.org/10.1175/BAMS-D-19-0335.1
- Wang, L., & Nakamura, N. (2015). Covariation of finite-amplitude wave activity and the zonal mean flow in the midlatitude troposphere: 1. Theory and application to the Southern Hemisphere summer. Geophysical Research Letters, 42(19), 8192-8200. https://doi.org/10.1002/ 2015GL065830
- Wang, L., Xu, P., Chen, W., & Liu, Y. (2017). Interdecadal variations of the Silk road pattern. Journal of Climate, 30(24), 9915–9932. https://doi. org/10.1175/JCLI-D-17-0340.1
- Webster, P. J., Moore, A. M., Loschnigg, J. P., & Leben, R. R. (1999). Coupled ocean-atmosphere dynamics in the Indian Ocean during 1997–98. Nature, 401(6751), 356-360. https://doi.org/10.1038/43848
- Webster, P. J., & Yang, S. (1992). Monsoon and Enso: Selectively interactive systems. Quarterly Journal of the Royal Meteorological Society, 118(507), 877-926. https://doi.org/10.1002/qj.49711850705
- Woollings, T., Barriopedro, D., Methven, J., Son, S. W., Martius, O., Harvey, B., et al. (2018). Blocking and its response to climate change. Current Climate Change Reports, 4(3), 287-300. https://doi.org/10.1007/s40641-018-0108-z
- Woollings, T., Hoskins, B., Blackburn, M., & Berrisford, P. (2008). A new Rossby wave-breaking interpretation of the North Atlantic oscillation. Journal of the Atmospheric Sciences, 65(2), 609-626. https://doi.org/10.1175/2007JAS2347.1
- Xavier, A., Kottayil, A., Mohanakumar, K., & Xavier, P. K. (2018). The role of monsoon low-level jet in modulating heavy rainfall events. International Journal of Climatology, 38(S1), https://doi.org/10.1002/joc.5390
- Xie, J., Hsu, P.-C., Lee, J.-Y., Wang, L., & Turner, A. G. (2024). Tropical intraseasonal oscillations as key driver and source of predictability for the 2022 Pakistan record-breaking rainfall event. npj Climate and Atmospheric Science, 7(1), 256. https://doi.org/10.1038/s41612-024-00809-9
- Yadav, R. K. (2024). The recent trends in the Indian summer monsoon rainfall. Environment, Development and Sustainability, 27(6), 13565-13579, https://doi.org/10.1007/s10668-024-04488-7
- Yadav, R. K., Srinivas, G., & Chowdary, J. S. (2018). Atlantic Niño modulation of the Indian summer monsoon through Asian jet. npj Climate and Atmospheric Science, 1(1), 23. https://doi.org/10.1038/s41612-018-0029-5
- Yan, X., Wang, L., Gerber, E. P., Castañeda, V., & Ho, K. Y. (2024). Traffic bottlenecks: Predicting atmospheric blocking with a diminishing flow capacity. Geophysical Research Letters, 51(19), e2024GL111035. https://doi.org/10.1029/2024GL111035
- Yanai, M., Esbensen, S., & Chu, J.-H. (1973). Determination of bulk properties of tropical cloud clusters from large-scale heat and moisture budgets. Journal of the Atmospheric Sciences, 30(4). https://doi.org/10.1175/1520-0469(1973)030(0611:dobpot)2.0.co;2
- Yin, J. H. (2005). A consistent poleward shift of the storm tracks in simulations of 21st century climate. Geophysical Research Letters, 32(18). https://doi.org/10.1029/2005GL023684
- Yoon, J. H., & Chen, T. C. (2005). Water vapor budget of the Indian monsoon depression. Tellus, Series A: Dynamic Meteorology and Oceanography, 57(5), 770. https://doi.org/10.3402/tellusa.v57i5.14737
- Yuan, X., Yang, K., Sun, J., Wang, Y., He, Y. Y., Zou, M. J., & Jiang, Y. Z. (2023). Why was Pakistan extreme precipitation stronger in 2022 than in 2010? Advances in Climate Change Research, 14(6), 913-920. https://doi.org/10.1016/j.accre.2023.11.016
- Zhang, R., & Delworth, T. L. (2005). Simulated tropical response to a substantial weakening of the Atlantic thermohaline circulation. Journal of Climate, 18(12), 1853-1860. https://doi.org/10.1175/JCLI3460.1

MAHENDRA ET AL. 29 of 29